



PERGAMON

Available online at www.sciencedirect.com

SCIENCE @ DIRECT®

Engineering Fracture Mechanics 70 (2003) 1809–1839

Engineering
Fracture
Mechanics

www.elsevier.com/locate/engfracmech

Cohesive crack model description of ductile to brittle size-scale transition: dimensional analysis vs. renormalization group theory

A. Carpinteri *, P. Cornetti, F. Barpi, S. Valente

Dipartimento di Ingegneria Strutturale e Geotecnica, Politecnico de Torino, Corso Duca degli Abruzzi 24, Torino 10129, Italy

Received 29 July 2002; received in revised form 6 February 2003; accepted 7 February 2003

Abstract

The present paper is a review of the research works carried out on the cohesive crack model and its applications at the Politecnico di Torino during the last decade. The topic encompasses experimental, numerical and theoretical aspects of the cohesive crack model. The research work followed two main directions. The *early work* concerns the development and the implementation of the cohesive crack model, which has been shown to be able to simulate experiments on concrete specimens and structures. It is referred to as the dimensional analysis approach, since it succeeds in capturing the ductile-to-brittle transition by increasing the structural size owing to the different physical dimensions of two material parameters: the tensile strength and the fracture energy.

On the other hand, the *later* research direction aims at extending the classical cohesive model to quasi-brittle materials showing (as they often do) fractal patterns in the failure process. This approach is referred to as the renormalization group (or fractal) approach and leads to a scale-invariant cohesive crack model. This model is able to predict the size effects even in tests where the classical approach fails, e.g. the direct tension test.

The two research paths, therefore, complete each other, allowing a deeper insight into the ductile-to-brittle transition usually detected when testing quasi-brittle material specimens or structures at different size-scales.

© 2003 Elsevier Science Ltd. All rights reserved.

Keywords: Cohesive crack; Concrete; Fractal geometry; Size-effect

1. Introduction

Concrete in tension exhibits *strain softening*, i.e., a negative slope in the *stress–deformation* diagram, due to microcracking and localization of the deformation in a narrow band, where energy dissipation occurs. The behaviour of the material outside this band is still linear and elastic. This phenomenon, observed experimentally by L'Hermite [1], Rusch and Hilsdorf [2], Hughes and Chapman [3], Evans and Marathe [4],

* Corresponding author. Tel.: +39-11-564-4850; fax: +39-11-564-4899.

E-mail address: alberto.carpinteri@polito.it (A. Carpinteri).

among others, must be taken into account in order to provide a good explanation of the behaviour of the material.

From the Continuum Mechanics viewpoint, strain softening represents a violation of Drucker's Postulate [5], as was pointed out by Maier [6,7] and Maier et al. [8]. These authors showed that, even in the absence of geometrical instability effects, the following phenomena may occur:

- loss of stability in the controlled load condition (*snap-through*);
- loss of stability in the controlled displacement condition (*snap-back*);
- *bifurcation* of the equilibrium path;
- *loss of uniqueness* of the solution in the incremental elasto-plastic response;
- *dependence* of the results on the type of mesh used in the numerical analysis.

A continuum described by strain-softening is also characterized by an imaginary wave speed or by the change of the equation of motion from hyperbolic to elliptic, as pointed out by Hadamard [9]. This confirms the difficulties involved in this constitutive relationship, as compared to the classical strain-hardening one.

The finite element method (FEM) was first applied to the problem of concrete cracking by Rashid [10], who adopted the so-called 'smeared crack model'. In this approach to the cracking process, the stress in the element was limited by the tensile strength of the material, beyond which point the stress registered a vertical drop to zero. Scanlon [11], among others, used a constitutive model in which the stress is reduced gradually to zero in a sequence of small stress drops, i.e., by introducing a strain-softening constitutive law. Softening was added in finite element codes and applied to a large number of problems, but it was discovered that the convergence properties were incorrect and the results strongly dependent on the mesh size. The problem was that the energy dissipated by cracking decreases with the refinement of the mesh and converges to zero. This trend, referred to as *spurious mesh sensitivity*, is physically unacceptable. By specifying the energy dissipated over cracking surfaces, it is possible to eliminate the mesh sensitivity. A relationship describing the softening damage must be introduced in the model; this can be done basically in two ways:

- by introducing a softening stress–crack opening displacement constitutive law, or
- by using a softening stress–strain relation for the material *included in a band around* the crack (the bandwidth is an additional parameter to be determined).

The first approach represents the basis of the 'cohesive crack model'; it involves the separation of the nodes of two adjacent elements belonging to the crack. The second refers to two models, not described here, referred to as the 'crack band model' and the 'non-local model' (see, for instance, [12,13]). These models are attractive because they involve only the modification of the classical constitutive relationship without requiring remeshing procedures.

The cohesive crack model is able to describe materials that exhibit a strain-softening type behaviour. The area under the closing stress vs. crack opening displacement curve represents the fracture energy \mathcal{G}_F assumed as a *material property*. This approach eliminates the mesh sensitivity. Mode I problems are characterized by the a priori knowledge of the crack trajectory, whilst in mixed-mode problems this is an additional unknown. In either case, the FEM represents an effective way to address crack propagation problems and phenomena such as size effect and ductile-to-brittle transition; it will be used later in this paper.

The cohesive crack model was initially proposed by Barenblatt [14,15] and Dugdale [16]. Subsequently, Dugdale's model was reconsidered by Bilby et al. [17], Willis [18], Rice [19], and utilized by Wnuk, who referred to it as the final stretch criterion [20]. Hillerborg et al. [21] proposed the 'fictitious crack model' in

order to study crack propagation in concrete. The crack is assumed to propagate when the stress at the crack tip reaches the tensile strength σ_u . When the crack opens, the stress is not assumed to fall to zero at once, but to decrease with increasing crack width w . The amount of energy absorbed per unit crack area (denoted here by \mathcal{G}_F) is:

$$\mathcal{G}_F = \int_0^{w_c} \sigma \, dw \quad (1)$$

and represents the area under the curve $\sigma-w$ (where w_c is the *critical displacement*, i.e., the distance between the crack surfaces, at which the interaction vanishes). Concrete is assumed to be linear elastic until σ_u is reached.

There are some similarities among Barenblatt's, Dugdale's, Rice's and Hillerborg's formulations: the crack tip faces close smoothly (the stress intensity factor K_I vanishes at the crack tip in mode I propagation) and the fracture process zone is of negligible thickness. On the other hand, the closing stresses in the fracture process zone are constant only in Dugdale's model, while the size of this zone is constant and small in comparison with the length of the main crack only in Barenblatt's model.

Again, with some modifications, the model was further applied by Wecharatana and Shah [22], Bažant and Oh [23], and Ingraffea and Gerstle [24]. More recently, the former terminology of cohesive crack model has been repropounded by Carpinteri [25–28], Carpinteri et al. [29–31] and the model has been used with this name by a number of researchers (for instance, Carpinteri and Valente [32], Cen and Maier [33], Elices et al. [34], among others).

Later on, in order to explain the size effects upon the parameters of the cohesive crack model, Carpinteri [35,36] applied fractal geometry concepts and described the influence of the microstructural disorder typical of most of quasi-brittle materials. The fractal approach was further developed by Carpinteri et al. [37,38]. Recently, an improvement of the cohesive crack model, the so-called (scale-invariant) *fractal cohesive crack model* [39], has been proposed and applied to interpret the most extensive experimental tensile data from concrete specimens tested over a broad range of scales [40,41].

Finally, the reader is referred to the following books [42–49] authored or edited by the first author of the present paper.

2. Basic concepts of the cohesive crack model

The basic assumption is the formation, as an extension of the real crack, of a *fictitious crack*, referred to as the process zone, where the material, albeit damaged, is still able to transfer stresses (Fig. 1).

The point separating the stress-free area, i.e., the real crack, from the process zone, is called real crack tip, whilst the point separating the process zone from the uncracked material is referred to as fictitious crack tip. The process zone represents the area in which energy dissipation takes place: it begins to form when the principal tensile stress reaches the material ultimate tensile strength, σ_u , in the direction perpendicular to the direction of the principal tensile stress. Furthermore, in the process zone, the stresses transferred by the material are decreasing functions of the displacement discontinuity, according to a proper *cohesive law* (linear in Fig. 2b), whilst in the uncracked zone the behaviour of the material is linear-elastic, as shown in Fig. 2a.

At the end of the fictitious crack, the stress will always be equal to the value of ultimate tensile strength. Thus, no singularities arise in the state of stress. In the model described so far, shearing stresses in the process zone are disregarded. The area under the $\sigma-w$ segment represents the fracture energy, \mathcal{G}_F , which, like the ultimate tensile strength, is usually considered as a property of the material. This assumption will be removed in Section 5.2.

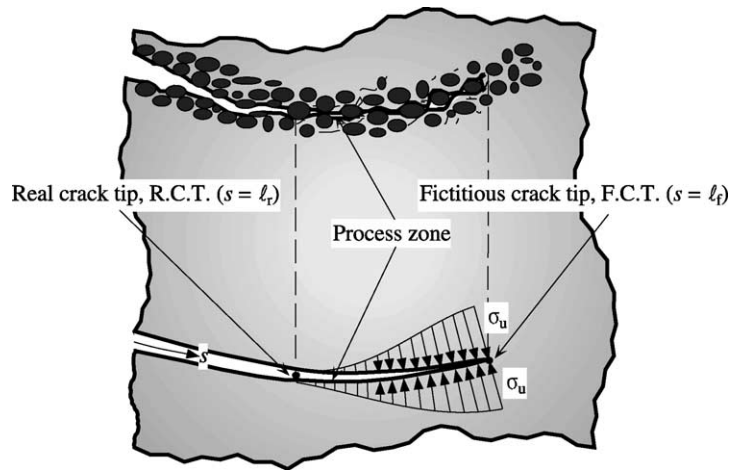


Fig. 1. Process zone (without shearing stresses).

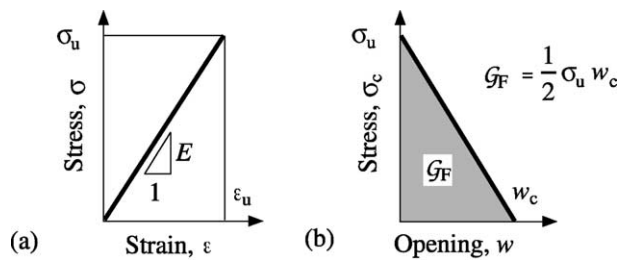


Fig. 2. Constitutive laws: (a) undamaged material and (b) process zone.

2.1. Elementary beam model

The linear elastic behaviour of an initially uncracked beam in three-point bending may be represented by the following dimensionless equation [27,50,51]:

$$\tilde{P} = \frac{4}{\lambda^3} \tilde{\delta} \tag{2}$$

where the dimensionless load and central deflection are given respectively by:

$$\tilde{P} = \frac{P\ell}{\sigma_u t h^2} \tag{3a}$$

$$\tilde{\delta} = \frac{\delta\ell}{\epsilon_u h^2} \tag{3b}$$

with ℓ , the beam span; h , the beam depth; t , the beam thickness and $\lambda = \ell/h$, the beam slenderness. Once the ultimate tensile strength is reached at the lower edge of the beam, a fracturing process in the central cross section is assumed to set in. Such a process admits of a limit-situation like that in Fig. 3.

The limit stage of the fracturing and deformation process may be considered as that of two rigid parts connected by the hinge A at the upper edge of the beam. The equilibrium of each part is ensured by the

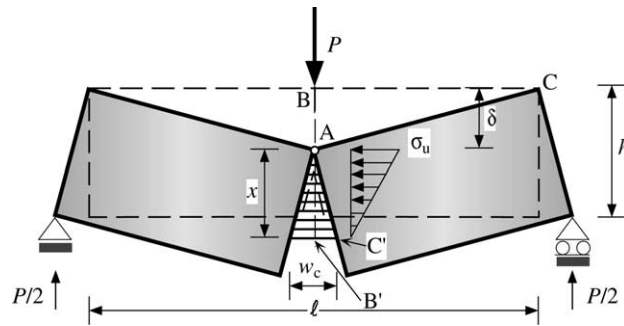


Fig. 3. Elementary beam model with cohesive forces.

external load, the support reaction and the closing cohesive forces (Fig. 3). The latter depend on the distance between the two interacting surfaces: as the distance w increases, the cohesive forces decrease until they vanish for $w > w_c$. The geometrical similarity of the triangles ABC and $AB'C'$ in Fig. 3 yields:

$$\frac{\delta}{\ell/2} = \frac{w_c/2}{x} \tag{4}$$

where x is the extension of the triangular distribution of the cohesive forces. Eq. (4) can be rearranged as follows:

$$x = \frac{w_c \ell}{4\delta} \tag{5}$$

The rotational equilibrium around point A is possible for each beam part only if the moments of support reaction and cohesive forces are equal:

$$\frac{P}{2} \frac{\ell}{2} = \frac{\sigma_u x t}{2} \frac{x}{3} \tag{6}$$

Recalling Eq. (5), the relation between load and deflection may be obtained:

$$P = \frac{\sigma_u t w_c^2}{24} \frac{\ell}{\delta^2} \tag{7}$$

Eq. (7) can be cast in dimensionless form:

$$\tilde{P} = \frac{1}{6} \left(\frac{\mathcal{G}_F}{\sigma_u h} \frac{\lambda^2}{\varepsilon_u \delta} \right)^2 = \frac{1}{6} \left(s_E \frac{\lambda^2}{\varepsilon_u \delta} \right)^2 \tag{8}$$

where $s_E = \mathcal{G}_F / (\sigma_u h)$ represents the *energy brittleness number* [25]. While the linear equation (2) describes the linear elastic behaviour of the initially uncracked beam, the hyperbolic equation (8) represents the asymptotic behaviour of the same beam when it is totally cracked. Eq. (2) is valid only for load values lower than that producing the ultimate tensile strength σ_u at the lower beam edge:

$$\tilde{P} \leq \frac{2}{3} \tag{9}$$

On the other hand, Eq. (8) is valid only for deflection values higher than that producing a cohesive zone of extension x equal to the beam depth h :

$$x \leq h \tag{10}$$

From Eqs. (5) and (10) it follows that:

$$\tilde{\delta} \geq \delta_2 = \frac{s_E \lambda^2}{2\varepsilon_u} \tag{11}$$

The bounds (9) and (11), upper for load and lower for deflection respectively, can be transformed into two equivalent bounds, both upper for deflection and load. Eqs. (3a) and (9) yield:

$$\tilde{\delta} \leq \delta_1 = \frac{\lambda^3}{6} \tag{12}$$

whereas Eqs. (8) and (11) yield:

$$\tilde{P} \leq \frac{2}{3} \tag{13}$$

Conditions (9) and (13) are identical. Therefore, a stability criterion for elastic-softening beams may be obtained by comparing Eqs. (11) and (12). When the two domains are separated, the two load–deflection branches (linear and hyperbolic) may be assumed to be connected by a regular curve, as in Fig. 4a.

On the other hand, when the two domains are partially overlapped, it is reasonable to assume that they are connected by a curve with highly negative or even positive slope (Fig. 4b). Unstable behaviour and catastrophic events (*snap-back*) may be possible for:

$$\frac{s_E \lambda^2}{2\varepsilon_u} \leq \frac{\lambda^3}{6} \tag{14}$$

and the brittleness condition for the three-point bending geometry becomes:

$$\frac{s_E}{\varepsilon_u \lambda} \leq \frac{1}{3} \tag{15}$$

Therefore, the system is brittle for low brittleness numbers s_E , high ultimate tensile strain ε_u , and high slenderness λ . It is therefore evident that the relative brittleness for a structure depends not only on material properties but also on the structural size and slenderness. The global brittleness of the beam can be defined as the ratio of the ultimate elastic energy contained in the body to the energy dissipated by fracture (see also [52]):

$$\text{Brittleness} = \frac{\frac{1}{2} P_u \delta_u}{\mathcal{G}_F \text{Area}} = \frac{\frac{1}{18} \sigma_u \varepsilon_u h t \ell}{\mathcal{G}_F h t} = \frac{1}{18} \left(\frac{s_E}{\varepsilon_u \lambda} \right)^{-1} \tag{16}$$

Such a ratio is higher than unity when:

$$\frac{s_E}{\varepsilon_u \lambda} \leq \frac{1}{18} \tag{17}$$

Eq. (17) represents a stricter condition for global structural brittleness compared with Eq. (15).

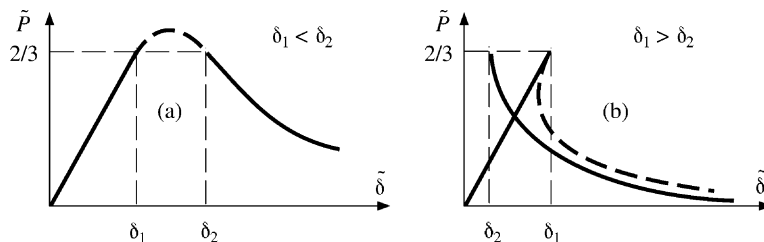


Fig. 4. Load vs. deflection diagrams: (a) ductile and (b) brittle condition ($\delta_1 = \lambda^3/6, \delta_2 = s_E \lambda^2/(2\varepsilon_u)$).

2.2. Beam model interpretation based on ultimate strength criterion and linear elastic fracture mechanics

Owing to the different physical dimensions of ultimate tensile strength σ_u and fracture toughness K_{IC} , under the usual conditions of engineering materials and fracture testing, scale effects are practically always present [28,50,53–55]. The key point is that the collapse can be governed by ultimate strength or by crack propagation: such a competition between types of collapse of a different nature becomes readily evident if we consider the ASTM formula for the three-point bending test (TPBT) evaluation of fracture toughness [56]:

$$K_I = \frac{P\ell}{th^{3/2}} f\left(\frac{a_0}{h}\right) \quad (18)$$

with

$$f\left(\frac{a_0}{h}\right) = 2.9\left(\frac{a_0}{h}\right)^{1/2} - 4.6\left(\frac{a_0}{h}\right)^{3/2} + 21.8\left(\frac{a_0}{h}\right)^{5/2} - 37.6\left(\frac{a_0}{h}\right)^{7/2} + 38.7\left(\frac{a_0}{h}\right)^{9/2} \quad (19)$$

For incipient crack propagation, $K_I = K_{IC}$; Eq. (18) becomes:

$$\frac{K_{IC}}{\sigma_u h^{1/2}} = s = \frac{P_{LEFM}\ell}{\sigma_u th^2} f\left(\frac{a_0}{h}\right) \quad (20)$$

where P_{LEFM} is the external load of brittle fracture and $s = K_{IC}/(\sigma_u h^{1/2})$ is the *static brittleness number* [53]. Rearranging Eq. (20) yields:

$$\frac{P_{LEFM}\ell}{\sigma_u th^2} = \frac{K_{IC}}{\sigma_u h^{1/2}} \frac{1}{f\left(\frac{a_0}{h}\right)} = \frac{s}{f\left(\frac{a_0}{h}\right)} \quad (21)$$

On the other hand, it is possible to consider the non-dimensional load of ultimate strength in a beam of depth $(h - a_0)$:

$$\frac{P_{US}\ell}{\sigma_u th^2} = \frac{2}{3} \left(1 - \frac{a_0}{h}\right)^2 \quad (22)$$

Eqs. (21) and (22) are plotted in Fig. 5 as functions of the relative crack depth a_0/h .

Whereas the former produces a set of curves as the brittleness number s is varied, the latter is represented by a single curve. It is evident that the ultimate strength collapse at the ligament precedes crack propagation for each initial crack depth when the brittleness number s is higher than the limit value $s_0 = 0.50$. For lower brittleness numbers, ultimate strength collapse precedes crack propagation only for crack depths outside a certain range. This means that a true LEFM collapse occurs only for comparatively low fracture toughnesses, high tensile strengths and/or large structural sizes. It is not the individual values of K_{IC} , σ_u and h that determine the nature of the collapse, but only their functions brittleness number—see Eq. (20). It is also possible to study the behaviour of the beam in terms of load–deflection curves. The deflection due to the elastic compliance of the uncracked beam is:

$$\delta_e = \frac{P\ell^3}{48EI} \quad (23)$$

where I is the inertial moment of the cross-section. On the other hand, the deflection due to the local crack compliance is [57]:

$$\delta_c = \frac{3}{2} \frac{P\ell^2}{th^2 E} g\left(\frac{a_0}{h}\right) \quad (24)$$

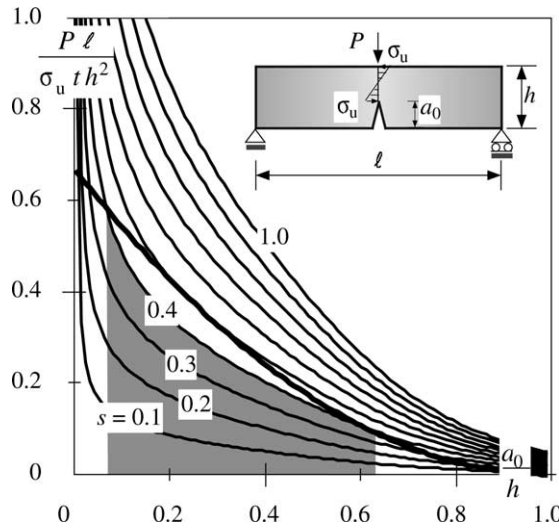


Fig. 5. Dimensionless load of crack instability vs. relative crack depth a_0/h .

with

$$g\left(\frac{a_0}{h}\right) = \left(\frac{\frac{a_0}{h}}{1 - \frac{a_0}{h}}\right) \left[5.58 - 19.57\left(\frac{a_0}{h}\right) + 36.82\left(\frac{a_0}{h}\right)^2 - 34.94\left(\frac{a_0}{h}\right)^3 + 12.77\left(\frac{a_0}{h}\right)^4 \right] \quad (25)$$

The superposition principle yields

$$\delta = \delta_e + \delta_c \quad (26)$$

and, in non-dimensional form

$$\frac{\delta \ell}{\varepsilon_u h^2} = \frac{P \ell}{\sigma_u t h^2} \left[\frac{1}{4} \left(\frac{\ell}{h}\right)^3 + \frac{3}{2} \left(\frac{\ell}{h}\right)^2 g\left(\frac{a_0}{h}\right) \right] \quad (27)$$

where $\varepsilon_u = \sigma_u/E$. The term in square brackets is the dimensionless compliance, which is a function of beam slenderness ℓ/h , as well as of crack depth, a_0/h . Some linear load–deflection diagrams are represented in Fig. 6, for varying crack depth a_0/h and for the fixed ratio $\ell/h = 4$.

By means of Eqs. (21) and (22) it is possible to determine the point of crack propagation as well as the point of ultimate strength on each linear plot of Fig. 6. Whereas the former depends on the brittleness number s , the latter is unique. The set of crack propagation points with constant s and varying crack depth represents a virtual load–deflection path, where point by point the load is always that producing crack instability. When the crack grows, the instability load decreases and the compliance increases, so that the product on the right-hand side of Eq. (27) may be either decreasing or increasing. The diagram of Fig. 6 shows the deflection decreasing (with the load) up to the crack depth $a_0/h \approx 0.30$ and then increasing (against the load). Therefore, whereas for $a_0/h > 0.30$ the load–deflection curve presents the usual softening trend with negative derivative, for $a_0/h < 0.30$ it presents a positive derivative. Such a branch could not be revealed by deflection-controlled testing, and the representative point would jump from the positive to the negative branch with a behaviour discontinuity. The set of ultimate tensile strength points, with varying crack depth, is represented by the thick line in Fig. 6. This line intersects the virtual crack propagation

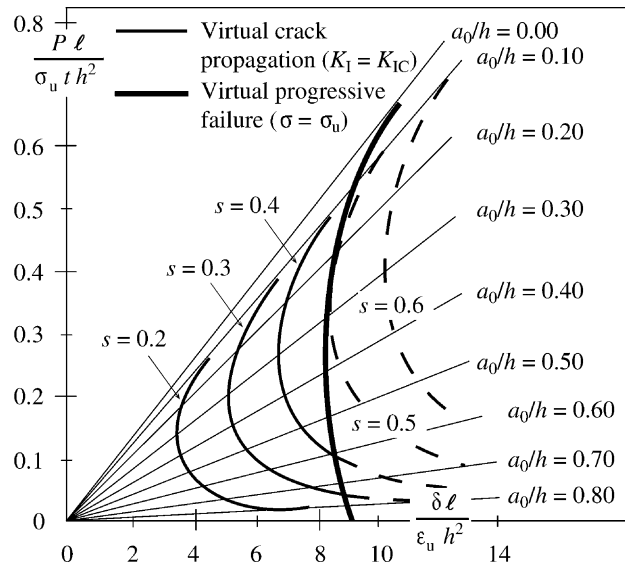


Fig. 6. Dimensionless load of crack instability vs. dimensionless deflection.

curves with $s \leq s_0 = 0.5$, which is analogous to what is shown in Fig. 5, and presents a slight indentation with $dP/d\delta > 0$.

3. Mode I problems—numerical simulations

The analyses discussed in this section concern the behaviour of concrete elements in mode I conditions (TPBT). For reasons of symmetry, the crack trajectory is known a priori. The numerical results, based on the cohesive model, were obtained using the finite element code (FRANA) fracture analysis [25–31]. An extensive series of analyses was carried out from 1984 to 1989 by Carpinteri and co-workers, and some of the results obtained are mentioned later [25–31]. The experimental results can be found in [58–60]. The cases described in the reference papers regard three ℓ/h ratios (4, 8 and 16), and four a_0/h ratios (0.00, 0.10, 0.30, 0.50) (see, for instance, Figs. 7 and 8). For each ratio, the response was analyzed for different values of the brittleness number, s_E , ranging from 2×10^{-2} to 2×10^{-5} . The concrete properties are listed in Table 1.

As can be seen from the diagrams, the brittleness number s_E has a decisive effect on the structural response of the element: by increasing s_E , the behaviour of the element changes from brittle to ductile, as anticipated at the end of the previous section. Hence, the structural response is not described by the parameters σ_u , \mathcal{G}_F and h independently, but rather by a combination of these parameters, as expressed by the brittleness number s_E .

A comparison between the results obtained with the FEM and those provided by the boundary element method can be found in [33,61]. The agreement between the results is excellent: both implementations of the cohesive model are able to describe snap-back phenomena.

3.1. Strain localization and apparent strength of initially uncracked beams

Some dimensionless load–deflection diagrams for a concrete-like material are plotted in Figs. 7 and 8. The specimen behaviour is brittle (snap-back) for low s_E numbers, i.e., for low fracture toughnesses \mathcal{G}_F ,

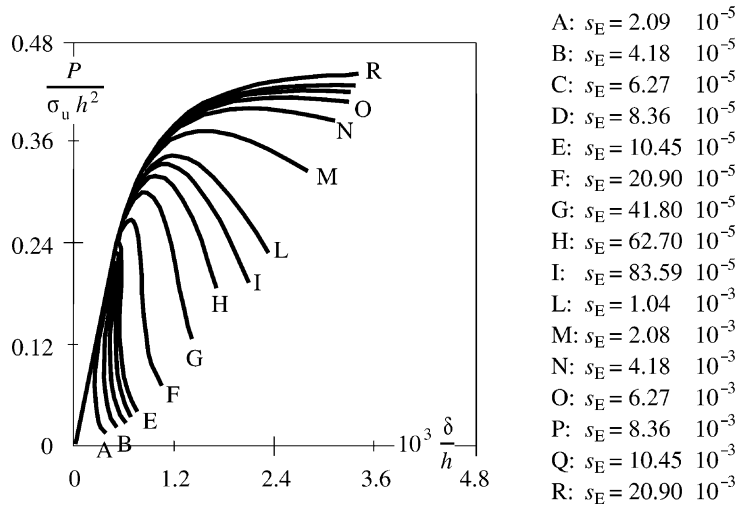


Fig. 7. Load vs. deflection curves, $a_0/h = 0.00$.

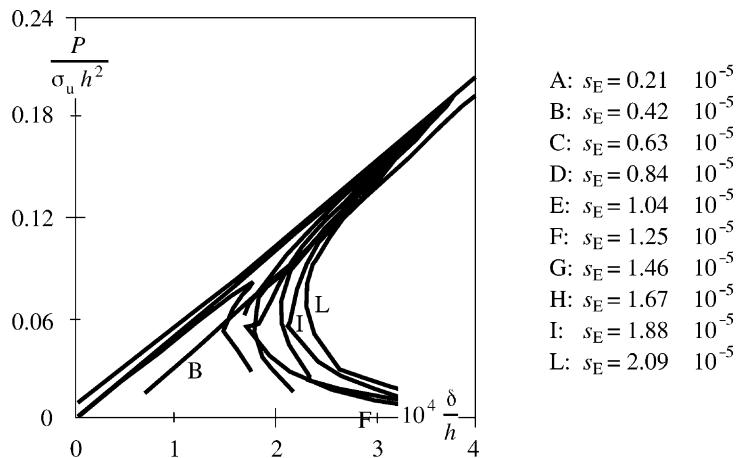


Fig. 8. Load vs. deflection curves, $a_0/h = 0.00$.

Table 1
Material properties (three point bending test)

E (MPa)	ν	σ_u (MPa)	ϵ_u
36 500	0.10	3.19	8.70×10^{-5}

high tensile strengths σ_u , and/or large sizes h . In Fig. 7, for $s_E \leq 10.45 \times 10^{-5}$, the P - δ curve presents a positive slope in the softening branch, and a catastrophic event occurs if the loading process is deflection-controlled. Such an indenting branch is not virtual only if the loading process is controlled by a monotonically increasing function of time, such as the displacement discontinuity across the crack [50,51].

On the other hand, Eq. (15) yields $s_E \leq 11.60 \times 10^{-5}$. Such a condition reproduces the one shown in Fig. 7 very accurately, whereas Eq. (17) appears too severe. When the post-peak behaviour is kept under control

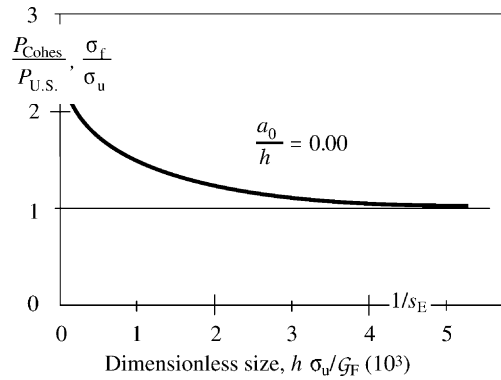


Fig. 9. Decrease in apparent strength by increasing the specimen size ($\lambda = 4$, $\epsilon_u = 0.87 \times 10^{-4}$).

up to complete structural separation, the area delimited by the load–deflection curve and deflection axis represents the product of fracture energy, \mathcal{G}_F , and initial cross-section area, $h \times t$.

The maximum loading capacity P_{Cohes} of the initially uncracked specimen with $\ell = 4h$ is obtained from Fig. 7. On the other hand, the maximum load P_{US} of ultimate strength is given by [50,51]:

$$P_{US} = \frac{2}{3} \frac{\sigma_u t h^2}{\ell} \tag{28}$$

The values of the ratio P_{Cohes}/P_{US} may also be regarded as the ratio of the apparent tensile strength σ_f (given by the maximum load P_{Cohes} and applying Eq. (28)) to the true tensile strength (considered as a material constant). It is evident from Fig. 9 that the results of the cohesive crack model tend to those of ultimate strength analysis for low s_E values:

$$\lim_{s_E \rightarrow 0} P_{Cohes} = P_{US} \tag{29}$$

Therefore, only for comparatively large specimen sizes can the tensile strength σ_u be obtained as $\sigma_u = \sigma_f$. With the usual laboratory specimens, an apparent strength higher than the true one is always found. As a limit case, for the size $h \rightarrow 0$ or fracture energy $\mathcal{G}_F \rightarrow \infty$ (elastic–perfectly plastic material in tension), i.e., for $s_E \rightarrow \infty$, the apparent tensile strength $\sigma_f \rightarrow 3\sigma_u$. In fact, in the centre of the beam, the uniform stress distribution (Fig. 10) produces a plastic hinge with a resistant moment M_{max} which is twice the classical moment of the birectangular limit stress distribution (elastic–perfectly plastic material in tension and compression).

The fictitious crack depth at the maximum load is plotted as a function of $1/s_E$ in Fig. 11. The brittleness increase for $s_E \rightarrow 0$ is evident also from this diagram, the process zone at $dP/d\delta = 0$ tending to disappear (brittle collapse), whereas it tends to cover the whole ligament for $s_E \rightarrow \infty$ (ductile collapse). On the other

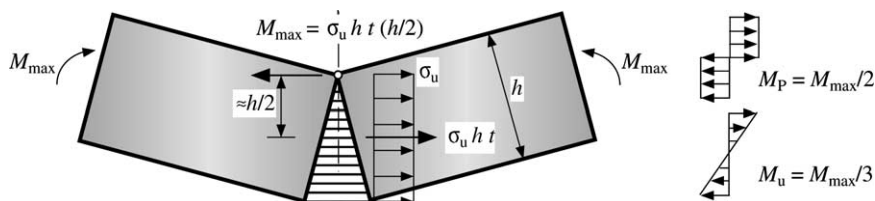


Fig. 10. Constant distribution of cohesive stresses.

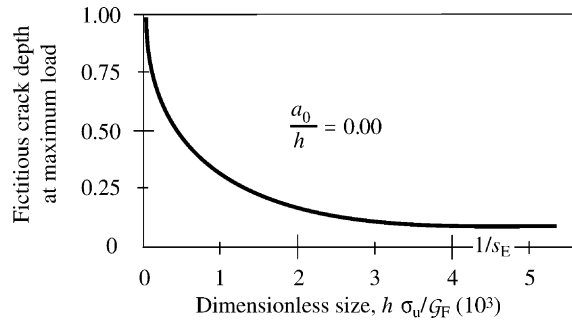


Fig. 11. Fictitious crack depth at maximum load as a function of specimen size ($\lambda = 4$, $\varepsilon_u = 0.87 \times 10^{-4}$).

hand, the real (or stress-free) crack depth at the maximum load is always zero for each value of s_E . This means that the slow crack growth does not start before the softening stage. Consequently, neither is slow crack growth found to occur nor does the cohesive zone develop before the peak, when $s_E \rightarrow 0$. Recalling once again Figs. 9 and 11, it is possible to state that, the smaller the brittleness number s_E , the more accurate the snap-back in reproducing the perfectly-brittle ultimate strength instability ($a_0/h = 0$).

3.2. Fracture toughness of initially cracked slabs

The mechanical behaviour of three-point bending slabs with initial cracks is investigated on the basis of the cohesive numerical model presented previously. The initial crack renders the specimen behaviour more ductile than in the case of the initially uncracked specimen [50,51] (see Figs. 12 and 13). The area delimited by the load–deflection curve and the deflection axis represents the product of fracture energy and initial ligament area, $(h - a_0) \times t$. The areas under the non-dimensional P – δ curves are thus proportional to the respective s_E numbers (Figs. 12 and 13).¹ This result is based upon the assumption that the energy dissipation occurs only on the fracture surface, whereas in reality energy is also dissipated in a damage volume around the crack tip as assumed in [62] and shown in [63].

The maximum loading capacity P_{Cohes} according to the cohesive crack model, is obtained from Figs. 12 and 13. On the other hand, the maximum load P_{LEFM} of brittle fracture can be obtained from linear elastic fracture mechanics (Eq. (20)), with $K_{\text{IC}} = (\mathcal{G}_F E)^{1/2}$ (plane stress condition). The values of the ratio $P_{\text{Cohes}}/P_{\text{LEFM}}$ are given as functions of the inverse of s_E in Fig. 14.

This ratio may also be regarded as the ratio of the fictitious fracture toughness (given by the maximum load P_{Cohes}) to the true fracture toughness (considered as a material constant). It is evident that for low s_E numbers the results of the cohesive crack model tend to those of linear elastic fracture mechanics [50,54]:

$$\lim_{s_E \rightarrow 0} P_{\text{Cohes}} = P_{\text{LEFM}} \quad (30)$$

and therefore, the maximum loading capacity can be predicted if the condition $K_I = K_{\text{IC}}$ is applied. It appears that the true fracture toughness K_{IC} of the material can be obtained only with very large specimens. In fact, with laboratory specimens, a fictitious fracture toughness lower than the true one is always measured.

¹ In the non-dimensional diagrams of Figs. 12 and 13 the area delimited is equal to $s_E \frac{t}{h} (1 - \frac{a_0}{h})$.

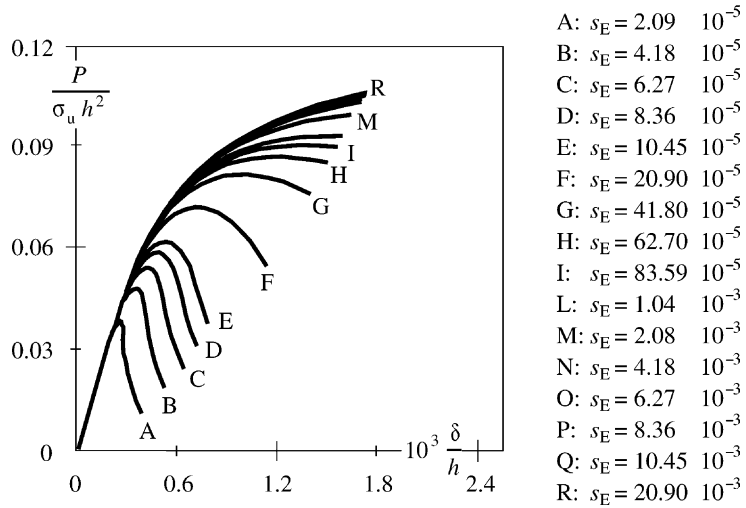


Fig. 12. Load vs. deflection curves, $a_0/h = 0.50$.

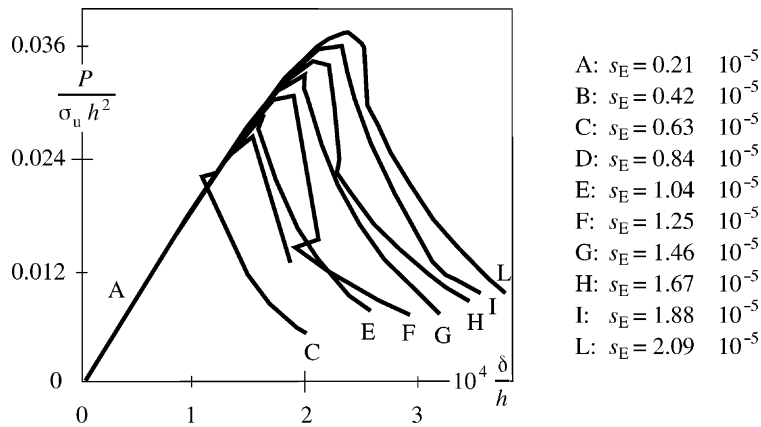


Fig. 13. Load vs. deflection curves, $a_0/h = 0.50$.

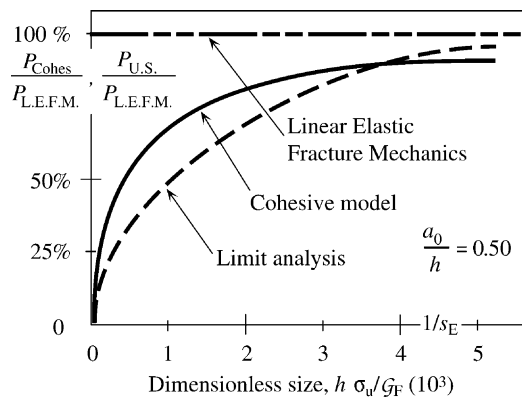


Fig. 14. Increase of fictitious toughness with increasing specimen size ($\lambda = 4$, $\epsilon_u = 0.87 \times 10^{-4}$).

4. Mixed-mode problems—numerical simulations

The analyses discussed in this section concern the behaviour of concrete elements in mixed-mode conditions (four-point shear test (FPST) with one or two notches and dam models). The crack trajectory is not known a priori, so that the finite element mesh must be modified at each step of crack propagation. All numerical simulations were performed with the aid of the Cohesive Crack Program (CCRAP) devised at the Politecnico di Torino by Valente and developed by Barpi in the last few years.

More information related to different mixed-mode conditions, namely the pull-out test, can be found in [64–68].

4.1. Four-point shear test with one notch

The testing set-up for the so-called FPST (or single-edge notched beam test) is shown in Fig. 15. A detailed description of these tests is provided in [69–72]. Concrete properties are illustrated in Table 2.

The load vs. crack mouth opening displacement diagrams are shown in Fig. 16. Figs. 17–19 show the load vs. displacement diagrams.

The quantities F_1 , δ_1 , F_2 , δ_2 are defined in Fig. 15. As can be seen, numerical and experimental results are in good agreement. On the other hand, the experimental results show a more rigid response, which can be explained by taking into account that the displacements were measured relative to a bar which neutralizes local strains in the constraints. Finally, Fig. 20 shows the mesh used in the numerical simulation when $h = 0.20$ m [73].

It can be seen that the smallest specimen broke into three parts, whereas the others into two. This trend was observed not only in the tests described in [70], but also in those illustrated in [69,74] and [71,72,75]. This phenomenon is taken into account by the cohesive model: Fig. 21 shows the mesh in the case of the propagation of the secondary crack, while Fig. 22 shows the corresponding load vs. displacement curve. For more details, the reader is referred to [76].

A brief overview of the different methods proposed to study this phenomenon is now given. The method proposed in [77] is based on a remeshing technique similar to the one illustrated in Figs. 20 and 21. This is a discrete-type model, and each crack is idealized by means of a line. Another approach [78], is represented by

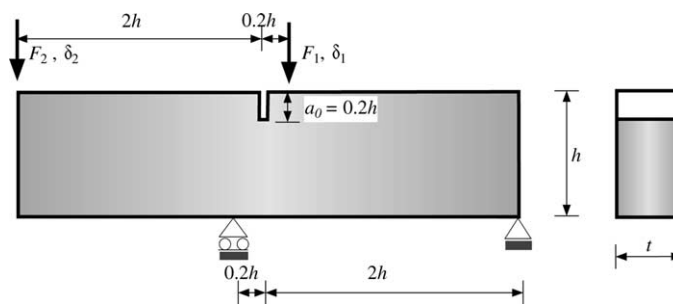


Fig. 15. FPST with one notch.

Table 2

Material properties (single-edge notched beam)

E (MPa)	ν	\mathcal{G}_F (N/m)	σ_u (MPa)
40 000	0.10	125	2.00

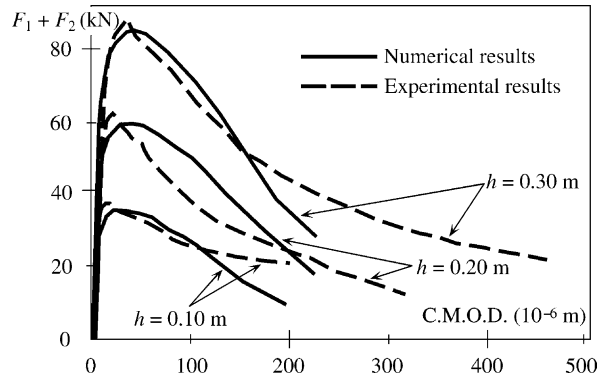


Fig. 16. Load vs. CMOD ($h = 0.10, 0.20, 0.30$ m).

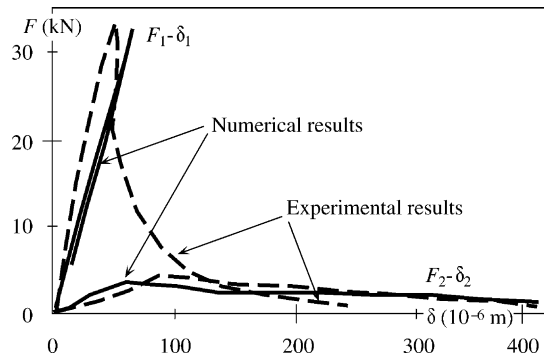


Fig. 17. Loads F_1, F_2 vs. displacements δ_1, δ_2 for $h = 0.10$ m.

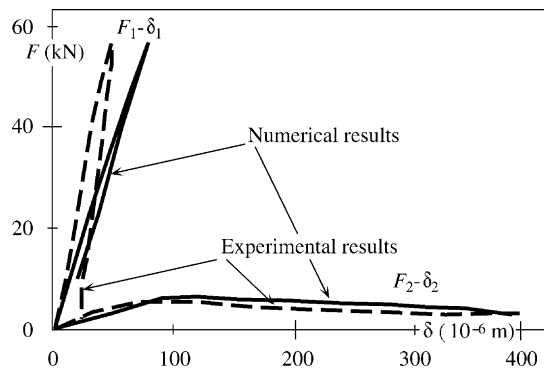


Fig. 18. Loads F_1, F_2 vs. displacements δ_1, δ_2 for $h = 0.20$ m.

the so-called ‘smeared crack model’. Whilst in the model proposed in [77] the crack trajectories are not connected with the direction of the mesh elements, in the smeared crack model they are affected by the arrangement of the elements. An approach which is similar to the foregoing one is that proposed in [79]: the crack trajectories are still affected by the type of mesh. In [80] the approach is still of the discrete type, with the crack trajectories correlated to the interface between adjacent elements.

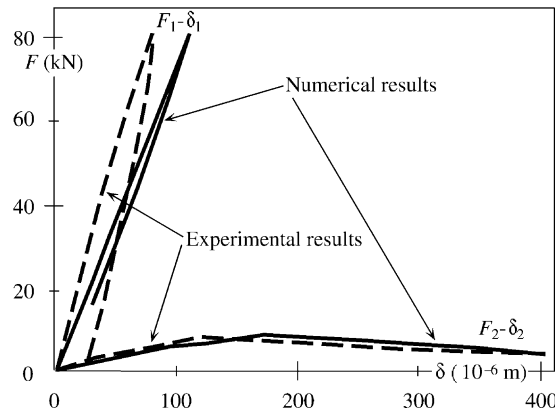


Fig. 19. Loads F_1, F_2 vs. displacements δ_1, δ_2 for $h = 0.30$ m.

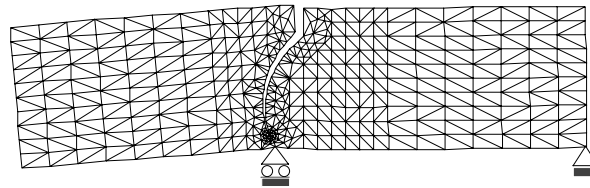


Fig. 20. Mesh used in the numerical simulation ($h = 20$ cm).

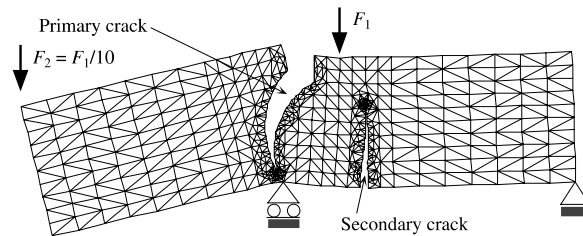


Fig. 21. Mesh for the case $h = 0.10$ m (specimen broken into three parts).

4.2. Gravity dam models

We shall now examine the behaviour of a gravity dam model, the dimensions of which are as shown in Fig. 23 [81]. The properties of the material used are listed in Table 3. In both cases, specimen thickness t was 30 cm, whereas the notch depth was taken to be 15 or 30 cm. Two constitutive laws were considered for the process zone: linear and bilinear. Fig. 24 presents the numerical and experimental results obtained for the specimens with 15-cm long notches.

When the state of stress at the tip of the fictitious crack is *isotropic*, i.e., characterized by the condition $\sigma_{xx} \approx \sigma_{yy}$, this makes the crack propagation criterion (based on the direction of principal tensile stress) inapplicable. For this reason, the analyses discussed in this section were stopped at this condition and are

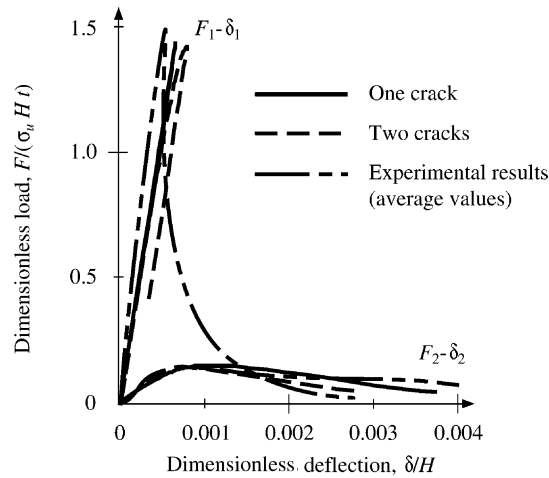


Fig. 22. Dimensionless loads vs. dimensionless displacements for the case $h = 0.10$ m (specimen broken into three parts).

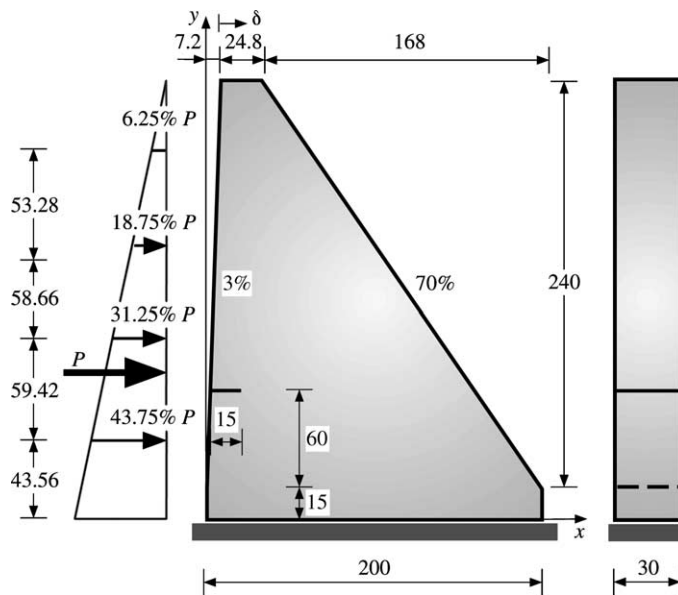


Fig. 23. Gravity dam model with notch length of 15 cm (dimensions in centimeters).

Table 3
Material properties (dam model)

E (MPa)	ν	\mathcal{G}_F (N/m)	σ_u (linear law) (MPa)	σ_u (bilinear law) (MPa)
35 700	0.10	184	3.60	4.32

necessarily incomplete. An alternative criterion is proposed in [82,83]. Numerical and experimental crack trajectories are shown in Fig. 25.

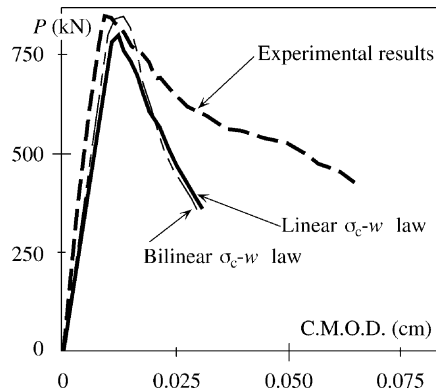


Fig. 24. Load vs. CMOD curves (notch length 15 cm).

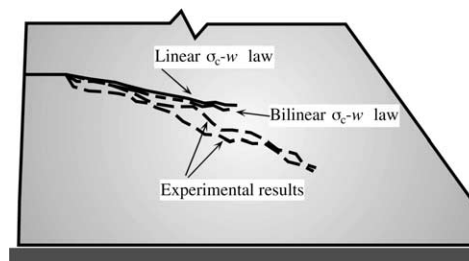


Fig. 25. Crack trajectories (notch length of 15 cm).

The study presented in [84] proposes an interesting comparison with the FEM and the diffused cracking model, while, in [85] an ‘anisotropic damaging model’ is proposed. A further and interesting comparison is based on an investigation [86] that sets forth the results obtained using different bilinear constitutive laws and different models of the shearing stresses in the process zone.

Concerning experimental tests on dam models, we mention the ones carried out by means of centrifugal equipment in order to simulate the behaviour of a 96-m high prototype. For more information (see [87–90]). The cohesive crack model has been extended to the study of crack propagation under constant load, coupling *creep* and *fracture*, in the case of mode I problems (see [91–95]). and mixed mode problems (see [96,97]). It has been further generalized by means of a viscous model based on a *fractional order rate law* to overcome the difficulties encountered using long chains of rheological elements, whose properties are difficult to determine (see [98–100]).

Due to the scatter in the material parameters, the same authors also examined the influence of *uncertainty* (or *imprecision*) in the material parameters by means of a *fuzzy-set* approach [101,102]. Given a value of vagueness in the material parameters, the fuzzy set theory makes it possible to evaluate the vagueness in the results avoiding the difficulties of a stochastic analysis.

5. Direct tension tests: the effect of the microstructural disorder

Dealing with the failure of unnotched specimens in tension, the cohesive crack model fails in predicting the size effects, which, nevertheless, rise. The explanation of the size effects upon tensile fracture properties

of concrete specimens, especially in direct tension tests, is an ongoing matter of discussion inside the scientific community. A sound approach to this problem has been proposed by Carpinteri since 1994 by means of *fractal geometry*.

5.1. The fractal approach

The fundamental reason of size effects rising in quasi-brittle material structures is *damage localization*. In the previous sections we showed how the cohesive crack model is able to catch this peculiar behaviour in several configurations. More generally, the cohesive crack model is able to simulate those tests where high stress gradients are present, i.e., tests on pre-notched specimens or in bending. In these cases, the cohesive crack model captures the ductile-to-brittle transition occurring by increasing the size of the structure. On the other hand, smaller but nevertheless relevant size effects are encountered in uniaxial tension tests on dog-bone shaped specimens, where much smaller stress gradients are present. In this case, size effects should be inherent to the material behaviour rather than to the stress gradient.

Apart from the tests carried out by Bažant and Pfeiffer [103] in a limited scale range (1:4), uniaxial tensile tests on dog-bone shaped specimens were performed by Carpinteri and Ferro [40], with controlled boundary conditions, in a scale range 1:16, and by van Mier and van Vliet [41], with rotating boundary conditions, in a scale range 1:32. The tests, in both cases, proved that the physical parameters characterizing the cohesive law are scale-dependent, thus showing the limits of Hillerborg's model. By increasing the size of the specimen, the peak of the cohesive law decreases while the tail rises. In other words, the tensile strength decreases while the fracture energy as well as the critical displacement increase.

A consistent explanation of the size effects affecting the cohesive law parameters in direct tension test was provided by Carpinteri [35,36] and by Carpinteri et al. [39] assuming *fractal* damage domains. This hypothesis is motivated by the disorder characterizing the microstructure of most quasi-brittle materials in a broad range of scales. Size effects in *uniaxial tensile* tests can therefore be seen as a consequence of the heterogeneous microstructure of concrete and rocks. Since the flaw distribution in quasi-brittle materials is often self-similar (i.e., it looks the same at different magnification levels), the microstructure can be correctly modelled by fractal sets.

Fractal sets are characterized by *non-integer* dimensions [104,105]. For instance, the dimension α of a fractal set in the plane can vary between 0 and 2. Accordingly, increasing the measure resolution, its length tends to zero if its dimension is smaller than 1 or tends to infinity if it is larger. In these cases, the length is a nominal, useless quantity, since it vanishes or diverges as the measure resolution increases. A finite measure can be achieved only using non-integer units, such as meters raised to α .

Analogously, if the stress and strain localization occurs in a fractal damaged zone, the nominal quantities (ultimate strength, critical strain, fracture energy) should depend on the resolution used to measure the set where stress, strain and energy dissipation take place. In the limit of a very high measure resolution, the stress and the strain should be infinite, while the dissipated energy should be zero. Finite values can be obtained only introducing fractal quantities, i.e., mechanical quantities with non-integer physical dimensions. On the other hand, if the measure resolution is fixed, the nominal quantities undergo size effects. More specifically, the fractal strain localization explains the observed increasing tail of the cohesive law as the specimen size increases (see [106]), i.e., it clarifies the scaling of the critical displacement w_c . Similarly, the fractal stress localization explains the experimentally observed decreasing peak in the cohesive law while increasing the specimen size, i.e., it clarifies the scaling of the tensile strength σ_u . Finally, the scaling of the fracture energy is a consequence of the invasive fractality of the set where energy dissipates (i.e. a fracture surface or a damaged band). According to the fractal approach, the scaling of the cohesive law parameters is represented by power laws, whose exponents are linked each other by a relation (as shown later).

Without entering the details, we wish to emphasize how the hypothesis of the fractal damage domain in quasi-brittle material failure is not a mathematical abstraction, since fractal patterns have been detected in

several experiments (see, for instance, [107,108]). Furthermore, for what concerns concrete, another explanation of the fractal features of the damaged zones has been recently derived from the analysis of the aggregate size distribution [109,110]. This *stereological* analysis confirmed the values of tensile strength and fracture energy power law exponents previously conjectured by Carpinteri based on dimensional analysis arguments [36].

The analyses of the fracture surfaces have shown that the fractal behaviour is more evident at the smaller scales. At the larger scales, the disorder and its influence onto the mechanical properties seem to diminish. While classical (i.e. self-similar) fractal sets cannot catch this trend, the self-affine fractals can. The scaling laws previously derived have been therefore extended to the self-affine case, leading to the definition of the so-called *multifractal scaling laws* [111,112] for tensile strength [37,113], for fracture energy [38,114], and, more recently, for critical displacement [110]. In this research field, these concepts have been applied not only to tensile tests, but also to explain the *R*-curve material behaviour [115] and to interpret the results of bending [116] and compression [117] tests. Finally, Carpinteri et al. [118,119] compared the size effect predictions provided by the fractal approach with the ones given by the gradient theory approach.

Another important research field has been recently opened by Carpinteri and Cornetti [120]. They have tried to generalize the classical differential equations of continuum mechanics to fractal media. Since the fractal functions, because of their irregularity, cannot be solutions of any differential equations, Carpinteri and Cornetti argued that suitable mathematical operators should replace the integro-differential operators of classical calculus [121]. The attention was drawn to the local fractional calculus operators recently introduced by Kolwankar [122] stemming from fractional calculus.² Here we just wish to point out that the order of differentiation is linked to the fractal dimension of the domain where the differential equations hold and that, by local fractional calculus, the authors succeeded in proving the principle of virtual work for fractal media [124–126].

We have previously seen that the cohesive model parameters are size-dependent. In order to get true material parameters, we are forced to introduce quantities with anomalous (non-integer) physical dimensions: the fractal tensile strength, the fractal critical strain and the fractal fracture energy. Thanks to their non-integer physical dimensions, they intrinsically introduce the fractal dimensions of the sets where stress, strain and energy dissipation localize.

In the next section, we will focus our attention upon these fractal mechanical quantities, in terms of which it is possible to define a scale-invariant (or fractal) cohesive law that represents a true material property. Together with the linear elastic constitutive law valid for the undamaged part of the material, the fractal cohesive law defines a material model that we call the (size-independent) *fractal cohesive crack model*. The model will be applied to the results of the tests carried out by Carpinteri and Ferro [127] and by van Mier and van Vliet [41], in order to prove the soundness of the fractal approach to the size effect prediction.

5.2. Scale-independent cohesive crack model

In order to introduce the fractal cohesive crack model, we have to consider separately the size effects on the three parameters characterizing the cohesive law.

Let us start analyzing the size effect on the tensile strength by considering a concrete specimen subjected to tension (Fig. 26a). Recent experimental results about the porous concrete microstructure [108] as well as a stereological analysis of concrete flaws [109] led us to believe that a consistent modelling of concrete

² Fractional calculus is the branch of the calculus dealing with integrals and derivatives of any order. See, for instance, the treatise [123].

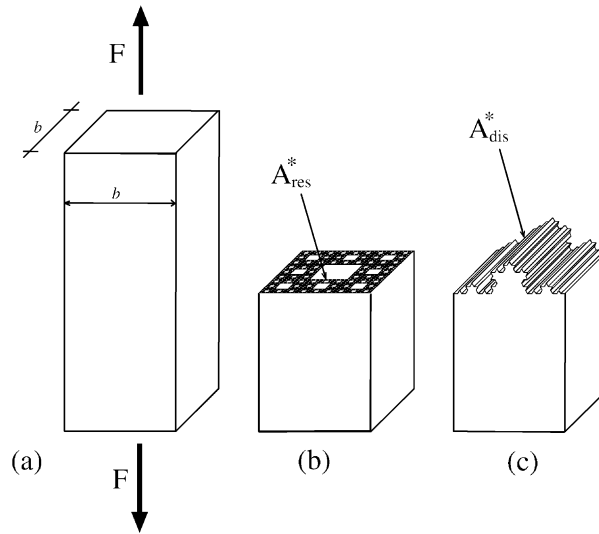


Fig. 26. A concrete specimen subjected to tension (a). Fractal localization of the stress upon the resistant cross section (b) and of the energy dissipation upon crack surface (c).

damage can be achieved by assuming that the rarefied resisting sections A_{res}^* in correspondence of the peak load can be represented by stochastic lacunar fractal sets with dimension $2 - d_\sigma$ ($d_\sigma \geq 0$). From fractal geometry, we know that the area of lacunar sets is scale-dependent and tends to zero as the resolution increases: the corresponding tensile strength should be infinite, which is physically meaningless. Finite measures can be obtained only with non-integer (fractal) dimensions. For the sake of simplicity, let us represent the specimen resistant cross-section as a Sierpinski carpet built on the square of side b (Fig. 26b). The fractal dimension of this lacunar domain is 1.893 ($d_\sigma = 0.107$). The assumption of Euclidean domain characterizing classical continuum mechanics states that the maximum load F is given by the product of the strength σ_u times the nominal area $A_0 = b^2$, whereas, in the present model, F equals the product of the (Hausdorff) fractal measure [105] $A_{res}^* \sim b^{2-d_\sigma}$ of the Sierpinski carpet times the *fractal tensile strength* σ_u^* [35]:

$$F = \sigma_u A_0 = \sigma_u^* A_{res}^* \tag{31}$$

where σ_u^* presents the anomalous physical dimensions $[F][L]^{-(2-d_\sigma)}$. Fractal tensile strength is the *true* material constant, i.e., it is a *scale-invariant*. From Eq. (31) we obtain the scaling law for tensile strength:

$$\sigma_u = \sigma_u^* b^{-d_\sigma} \tag{32}$$

i.e. a power law with negative exponent $-d_\sigma$. Eq. (32) represents the negative scale effect on tensile strength, experimentally revealed by several authors. Experimental and theoretical results allow us to affirm that d_σ can vary between the lower limit 0—canonical dimensions for σ_u^* and absence of size effect on tensile strength—and the upper limit $1/2 - \sigma_u^*$ with the physical dimensions of a stress-intensity factor and maximum size effect on tensile strength (as in the case of LEFM).

Secondly, let us consider the work W necessary to break a concrete specimen of cross section b^2 (Fig. 26a). It is equal to the product of the fracture energy \mathcal{G}_F times the nominal fracture area $A_0 = b^2$. On the other hand, the surface where energy is dissipated is not a flat cross-section: it is a crack surface, whose area A_{dis} diverges as the measure resolution tends to infinity because of its roughness at any scale. Therefore, the

fracture energy should be zero, which is physically meaningless. Finite values of the measure of the set where energy is dissipated can be achieved only via non-integer fractal dimensions. For the sake of simplicity, let us represent the crack surface as a von Kock surface built on the square of side b (Fig. 26c). The fractal dimension of this invasive domain is 2.262, i.e. $2 + d_g$ ($d_g = 0.262$). The classical cohesive crack model states that the failure work W is given by the product of the fracture energy \mathcal{G}_F times the nominal area $A_0 = b^2$, whereas, in the present model, W equals the product of the fractal (Hausdorff) measure [105] $A_{\text{dis}}^* \sim b^{2+d_g}$ of the von Kock surface times the *fractal fracture energy* \mathcal{G}_F^* [35]:

$$W = \mathcal{G}_F A_0 = \mathcal{G}_F^* A_{\text{dis}}^* \tag{33}$$

$$\mathcal{G}_F = \mathcal{G}_F^* b^{d_g} \tag{34}$$

\mathcal{G}_F^* is the true scale invariant material parameter, whereas the nominal value \mathcal{G}_F is subjected to a scale effect described by a positive power law.

Now we turn our attention to the deformation inside the zone where damage localizes (the so-called damaged band). We assume that the strain field presents fractal patterns. This could appear strange at a first glance; on the contrary, fractal strain distributions are rather common in material science. For instance, in some metals, the slip-lines develop with typical fractal patterns [128]. Fractal crack networks develop also in dry clay [129] or in old paintings under tensile stresses due to shrinkage. Thus, as representative of the damaged band, consider now the simplest structure, a bar subjected to tension (Fig. 27a), where, at the maximum load, dilation strain tends to concentrate into different softening regions, while the rest of the body undergoes elastic unloading.

Assume, for instance, that the strain is localized at cross-sections whose projections onto the longitudinal axis are provided by the triadic Cantor set, whose dimension is $\ln 2 / \ln 3 = 0.639$. The displacement function at rupture can be represented by a Cantor staircase graph, sometimes also called devil's staircase (Fig. 27a). The strain defined in the classical manner is meaningless in the singular points, where it diverges.

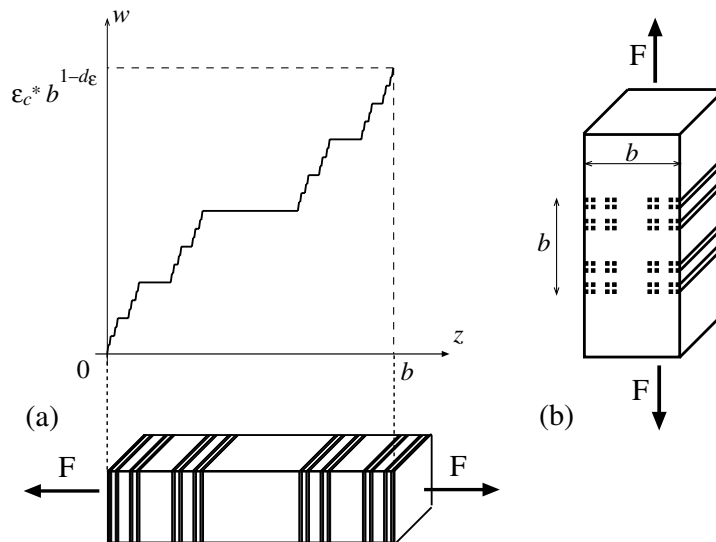


Fig. 27. Fractal localization of the strain (a) and of the energy dissipation inside the damaged band (b).

This drawback can be overcome by introducing a fractal strain. Let us indicate with $1 - d_e$ ($d_e \geq 0$) the fractal dimension of the lacunar projection of the cracked sections (in this case $d_e = 0.361$). According to the fractal measure of the damage line projection, the total elongation w_c of the band at rupture must be given by the product of the Hausdorff measure $b^* \sim b^{(1-d_e)}$ of the Cantor set times the *critical fractal strain* ε_c^* , while in classical continuum mechanics it equals the product of the length b times the critical strain ε_c :

$$w_c = \varepsilon_c b = \varepsilon_c^* b^{(1-d_e)} \tag{35}$$

$$\varepsilon_c = \varepsilon_c^* b^{-d_e} \tag{36}$$

where ε_c^* has the anomalous physical dimension $[L]^{d_e}$. The fractal critical strain is the true material constant, i.e. it is the only scale-invariant parameter governing the kinematics of the crack band. On the other hand, Eq. (35) states that the scaling of the critical displacement is described by a power law with positive exponent $(1 - d_e)$. The fractional exponent d_e is intimately related to the degree of disorder in the mesoscopic damage process. When d_e varies from 0 to 1, the kinematical control parameter ε_c^* moves from the canonical critical strain ε_c —dimensionless $[L]^0$ —to the critical crack opening displacement w_c —of dimension $[L]^1$. Therefore, when $d_e = 0$ (diffused damage, ductile behaviour), one obtains the classical response, i.e. collapse governed by the strain ε_c , independently of the bar length. In this case, continuum damage mechanics holds, and the critical displacement w_c is subjected to the maximum size effect ($w_c \propto b$). On the other hand, when $d_e = 1$ (localization of damage onto isolated sections, brittle behaviour) traditional fracture mechanics holds and the collapse is governed by the critical opening displacement w_c , which is size-independent as in the usual cohesive model.

The three scaling laws (32), (34) and (35) of the cohesive parameters are not completely independent of each other. In fact, there is a relation among the scaling exponents that must be always satisfied. This means that, when two exponents are given, the third follows from the first two. In order to get this relation, suppose, for instance, to know d_σ and d_e . Generalizing Eqs. (32) and (35) to the whole softening regime, we get $\sigma = \sigma^* b^{-d_\sigma}$ and $w = \varepsilon^* b^{(1-d_e)}$. These relationships can be considered as changes of variables and applied to the integral definition of the fracture energy:

$$\mathcal{G}_F = \int_0^{w_c} \sigma dw = b^{1-d_e-d_\sigma} \int_0^{\varepsilon_c^*} \sigma^* d\varepsilon^* = \mathcal{G}_F^* b^{1-d_e-d_\sigma} \tag{37}$$

Eq. (37) highlights the effect of the structural size on the fracture energy, as Eq. (34) does. Therefore, comparing Eqs. (34) and (37), we get the relation among the exponents:

$$d_\sigma + d_e + d_g = 1 \tag{38}$$

From a physical point of view, note that the geometrical relationship (38) states that, after the peak load, energy is dissipated over the infinite lacunar sections where softening takes place inside the damage band (Fig. 27b). This statement is not the same as considering the fractal crack surface (Fig. 26c) as the region where dissipation takes place. It is nevertheless equivalent since it yields the same power law scaling (34), the fractal dimensions of the dissipation domains being larger than 2 in both cases.

As shown above, d_e can get all the values inside the interval $[0, 1]$. Therefore, Eq. (38) provides a strict restriction to the maximum degree of disorder, confirming that the sum of d_σ and d_g is always lower than 1, as previously asserted by Carpinteri through dimensional analysis arguments [36]. It must be pointed out, however, that experiments provided always values for d_σ and d_g comprised between 0 and 1/2.

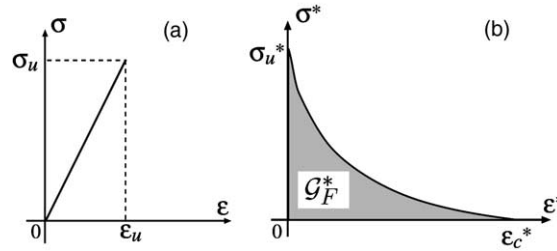


Fig. 28. Fractal cohesive model.

It is interesting to note, from Eq. (37), how the fractal fracture energy \mathcal{G}_F^* can be obtained as the area below the fractal softening stress–strain diagram (Fig. 28b). During the softening regime, i.e. when dissipation occurs, σ^* decreases from the maximum value σ_u^* to 0, while ε^* grows from 0 to ε_c^* . In the meantime, the non-damaged parts of the bar undergo elastic unloading (Fig. 28a). We call the $\sigma^*-\varepsilon^*$ diagram the scale-independent or *fractal cohesive law*. Contrarily to the classical cohesive law, which is experimentally sensitive to the structural size, this curve should be an exclusive property of the material, it being able to capture the fractal nature of the damage process. The couple of constitutive laws $\sigma-\varepsilon$ and $\sigma^*-\varepsilon^*$ (Fig. 28) define the *scale-invariant (fractal) cohesive crack model*.

In order to validate the model, it has been applied to the data obtained in 1994 by Carpinteri and Ferro [40,127] for tensile tests on dog-bone shaped concrete specimens of various sizes under controlled boundary conditions (Fig. 29a). They interpreted the size effects on the tensile strength and the fracture energy by fractal geometry. Fitting the experimental results, they found the values $d_\sigma = 0.14$ and $d_g = 0.38$. Some of the $\sigma-\varepsilon$ (stress vs. strain) and $\sigma-w$ diagrams are reported respectively in Fig. 29b and c, where w is the displacement localized in the damaged band, obtained by subtracting, from the total one, the displacement due to elastic and inelastic pre-peak deformation. Eq. (38) yields $d_\varepsilon = 0.48$, so that the fractal cohesive laws can be plotted in Fig. 29d. As expected, all the curves related to the single sizes tend to merge in a unique, scale-independent cohesive law. The overlapping of the cohesive laws for the different sizes proves the soundness of the fractal approach to the interpretation of concrete size effects.

More recently, van Mier and van Vliet [41] accurately performed tensile tests on dog-bone shaped concrete specimens over a wide scale range (1:32) under rotating boundary conditions (Fig. 31a). In Fig. 31b, the stress vs. strain diagrams are reported for different specimen sizes: note the ductile-to-brittle transition represented by the steeper negative softening slope for the larger sizes. In addition, van Mier and van Vliet plotted the cohesive law for specimens of different sizes and found that, increasing the specimen size, the peak of the curve decreases whereas the tail rises [106]. In other words, σ_u decreases whereas w_c and \mathcal{G}_F increase, thus confirming the predictions of the fractal model.

The authors are aware that the fractal cohesive law can be determined only from a set of experiments over a wide range of sizes. Nevertheless, they think that laboratory tests on different size specimens should be performed in order to get the fractal parameters and to extrapolate the nominal values of the material parameters for real scale structures.

A preliminary analysis of the data obtained by van Mier and van Vliet [41] was *also* performed according to the fractal cohesive model. The average values obtained for the different specimen sizes were considered in [110]. The data of the smallest specimen size ($D = 50$ mm) were not *taken into account*, since, as stated in [131], secondary effects are present that bias the results. For such a small size, in fact, the influence of the largest grain and the wall effect are stronger, while the degrees of the hydration is lower compared to larger specimens. All these facts explain the low strength values obtained for the smallest size: hence, their results should be considered with reservation.

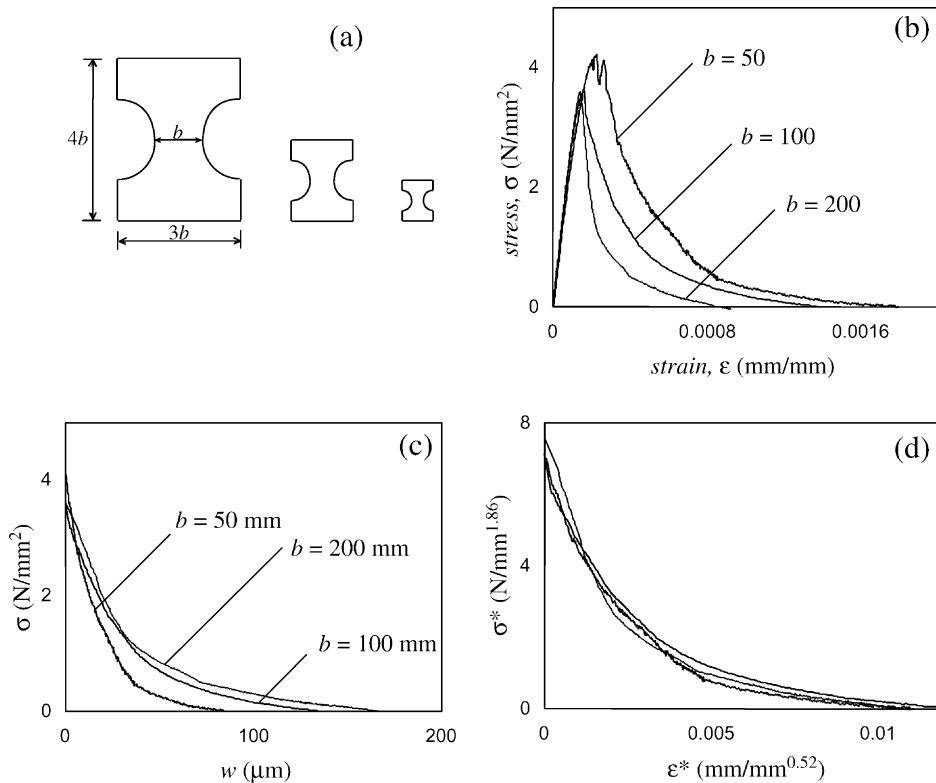


Fig. 29. Tensile tests on dog-bone shaped concrete specimens (a) by Ferro [130]: (b) stress–strain diagrams, (c) cohesive law diagrams and (d) fractal cohesive law diagrams.

For what concerns the fracture energy, van Mier and van Vliet were not able to obtain the whole tail of the softening branch for the specimens of the larger sizes. In order to obtain the value of the fracture energy, they completed the cohesive laws via a linear extrapolation. This procedure, although rigorous, leads to an underestimate of the computed fracture energy since it does not respect the concavity of the curve. Therefore, we decided to complete the cohesive law diagrams in a somehow arbitrary way maintaining the concave shape for all the specimen sizes (Fig. 31c). Observing the intercepts of the curves with the axes, it is evident that the higher is the peak, the shorter is the tail.

Linear regressions in the bilogarithmic plots of tensile strength and fracture energy vs. specimen cross section size were performed (Fig. 30). These regressions yielded [110] respectively a fractal fracture energy \mathcal{G}_F^* equal to $9.22 \times 10^{-2} \text{ N mm}^{-1.09}$ and a fractal tensile strength σ_u^* equal to $6.42 \text{ N mm}^{-1.82}$, with fractal exponents $d_g = 0.09$ and $d_\sigma = 0.18$. The correlation coefficients appear to be respectively $R_g = 0.995$ and $R_\sigma = 0.990$; their values close to unity prove the soundness of the power law scaling. Relation (38) among the scaling exponents yields $d_e = 0.73$, so that the fractal cohesive laws can be plotted in Fig. 31d. Once again the superposition of the different plots denotes the validity of the fractal cohesive model. In particular, note the low scattering of the intercepts with the horizontal and vertical axes in comparison with the ones in Fig. 31c: they represent respectively the fractal critical strain ϵ_c^* and the fractal tensile strength σ_u^* , while the area subtended by the fractal cohesive law diagrams provides \mathcal{G}_F^* . An even clearer representation is reported in Fig. 32, where different scales are used for low or high values of both the axes coordinates.

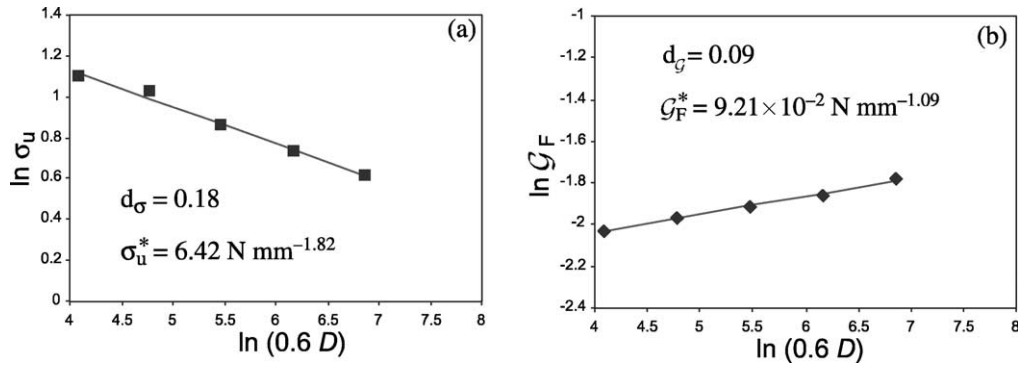


Fig. 30. Tensile strength (a) and fracture energy (b) vs. specimen size: experimental data by van Vliet [131] and linear interpolation in the bilogarithmic plot.

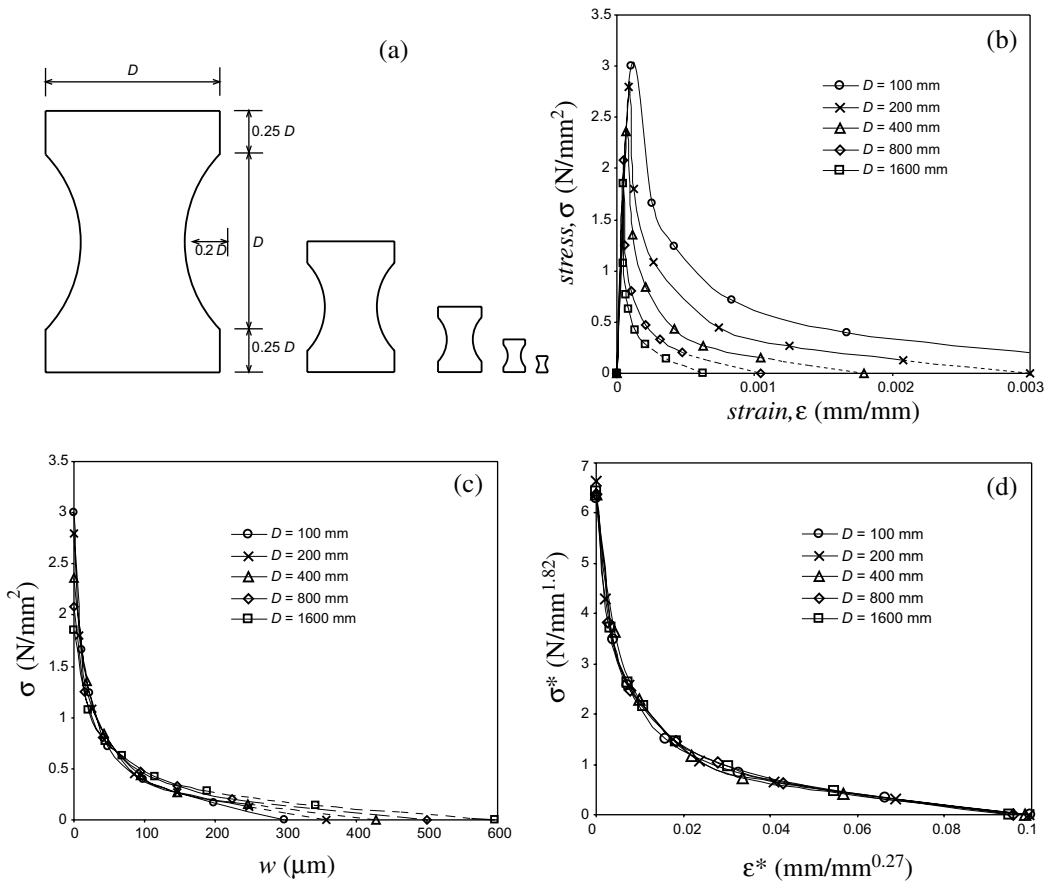


Fig. 31. Tensile tests on dog-bone shaped concrete specimens (a) by van Vliet [131]: (b) stress–strain diagrams, (c) cohesive law diagrams and (d) fractal cohesive law diagrams (d). The dashed lines refer to extrapolated values.

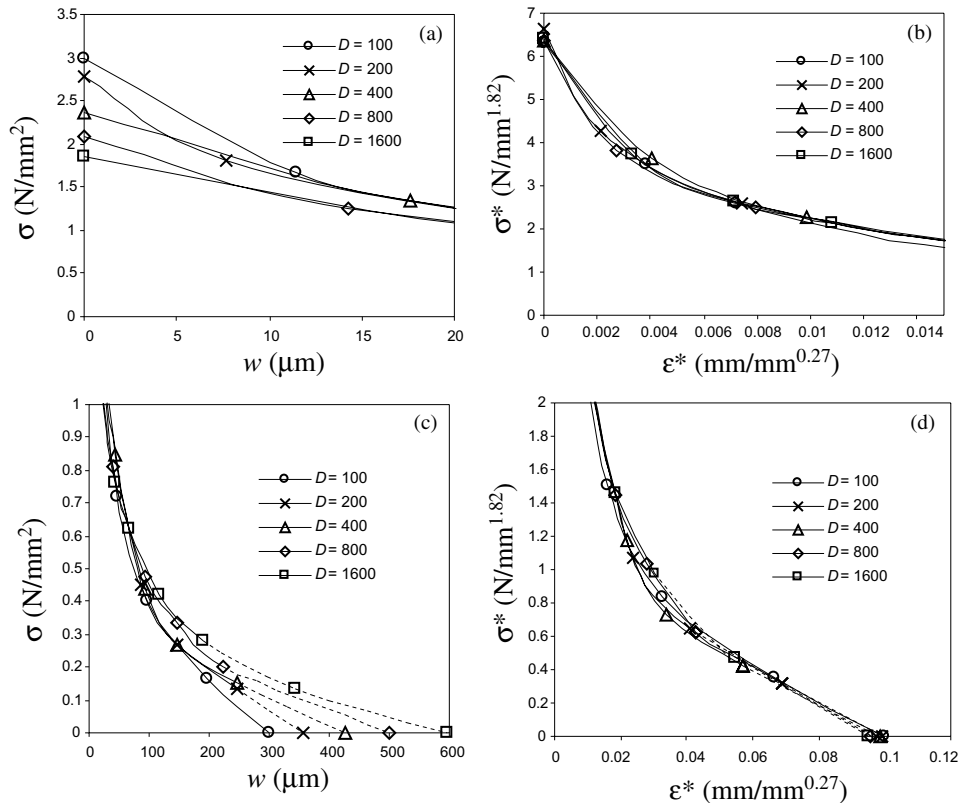


Fig. 32. Details of the peak (a) and of the tail (c) of the cohesive law diagrams. Details of the peak (b) and of the tail (d) of the fractal cohesive law diagrams. The dashed lines refer to extrapolated values.

Acknowledgements

Support by the MIUR and the EC-TMR Contract no. ERBFMRXCT 960062 is gratefully acknowledged by the authors.

References

- [1] L'Hermite R. What do we know about the plastic deformation and creep of concrete? RILEM Bull 1959;1:22–51.
- [2] Rusch H, Hilsdorf H. Deformation characteristics of concrete under axial tension. Munich, Bericht: Voruntersuchungen; 1963. p. 44.
- [3] Hughes BP, Chapman BP. The complete stress–strain curve for concrete in direct tension. RILEM Bull 1966;30:95–7.
- [4] Evans RH, Marathe MS. Microcracking and stress–strain curves for concrete in tension. Mater Struct 1968;1:61–4.
- [5] Drucker DC. Some implications of work-hardening and ideal plasticity. Quart Appl Math 1950;7:411–8.
- [6] Maier G. Behaviour of elastic–plastic trusses with unstable bars. J Engng Mech (ASCE) 1966;92:67–91.
- [7] Maier G. Incremental plastic analysis in the presence of large displacements and physical instabilizing effects. Int J Solids Struct 1971;7:345–72.
- [8] Maier G, Zavelani A, Dotreppe JC. Equilibrium branching due to flexural softening. J Engng Mech (ASCE) 1973;89:897–901.
- [9] Hadamard J. Leçons sur la Propagation des andes. Paris: Hermann; 1907.
- [10] Rashid YR. Analysis of prestressed concrete pressure vessels. Nucl Engng Des 1968;7:334–55.

- [11] Scanlon A. Time-dependent deflection of reinforced concrete slabs. PhD thesis, University of Alberta, Edmonton, Canada, 1971.
- [12] Bažant ZP. Mechanics of distributed cracking. *Appl Mech Rev (ASME)* 1986;309.
- [13] Bažant ZP, Gopalaratnam VS. Fracture mechanics of concrete: concepts, models and determination of material properties. In: Bažant ZP, editor. *Fracture mechanics of concrete structures*. The Netherlands: Elsevier Applied Science; 1992. p. 1–140.
- [14] Barenblatt GI. The formation of equilibrium cracks during brittle fracture: general ideas and hypotheses. *J Appl Math Mech* 1959;23:622–36.
- [15] Barenblatt GI. The mathematical theory of equilibrium cracks in brittle fracture. *Adv Appl Mech* 1962;7:55–129.
- [16] Dugdale DS. Yielding of steel sheets containing slits. *J Mech Phys Solids* 1960;8:100–14.
- [17] Bilby BA, Cottrell AH, Swinden KH. The spread of plastic yield from a notch. *Proc Royal Soc A* 1963;272:304–14.
- [18] Willis JR. A comparison of the fracture criteria of Griffith and Barenblatt. *J Mech Phys Solids* 1967;15:151–62.
- [19] Rice JR. A path independent integral and the approximate analysis of strain concentration by notches and cracks. *J Appl Mech* 1968;15:379–86.
- [20] Wnuk MP. Quasi-static extension of a tensile crack contained in viscoelastic–plastic solid. *J Appl Mech* 1974;41:234–42.
- [21] Hillerborg A, Modeer M, Petersson PE. Analysis of crack formation and crack growth in concrete by means of fracture mechanics and finite elements. *Cem Concr Res* 1976;6:773–82.
- [22] Wecharatana M, Shah SP. Prediction of non-linear fracture process zone in concrete. *J Engng Mech (ASCE)* 1983;109:1231–46.
- [23] Bažant ZP, Oh BH. Concrete fracture via stress–strain relations. Technical Report 81-10/665c, Center for Concrete and Geomaterials, Northwestern University, 1981.
- [24] Ingraffea AR, Gerstle WH. Nonlinear fracture models for discrete crack propagation. In: Shah SP, editor. *NATO: Advanced research workshop on application of fracture mechanics to cementitious composites*. Dordrecht: Martinus Nijhoff; 1984. p. 171–209.
- [25] Carpinteri A. Interpretation of the Griffith instability as a bifurcation of the global equilibrium. In: Shah SP, editor. *Application of fracture mechanics to cementitious composites*. The Netherlands: Martinus Nijhoff; 1985. p. 284–316.
- [26] Carpinteri A. Cusp catastrophe interpretation of fracture instability. *J Mech Phys Solids* 1989;37:567–82.
- [27] Carpinteri A. Decrease of apparent tensile and bending strength with specimen size: two different explanations based on fracture mechanics. *Int J Solids Struct* 1989;25:407–29.
- [28] Carpinteri A. Post-peak and post-bifurcation analysis on cohesive crack propagation. *Engng Fract Mech* 1989;32:265–78.
- [29] Carpinteri A, Di Tommaso A, Fanelli M. Influence of material parameters and geometry on cohesive crack propagation. In: Wittmann FH, editor. *Fracture toughness and fracture energy of concrete*. Elsevier Science Publisher; 1985. p. 117–35.
- [30] Carpinteri A, Colombo G, Giuseppetti G. Accuracy of the numerical description of cohesive crack propagation. In: Wittmann FH, editor. *Fracture toughness and fracture energy of concrete*. Elsevier Science Publisher; 1985. p. 189–95.
- [31] Carpinteri A, Di Tommaso A, Ferrara G, Melchiorri G. Experimental evaluation of concrete fracture energy through a new identification method. In: Wittmann FH, editor. *Fracture toughness and fracture energy of concrete*. Elsevier Science Publisher; 1985. p. 423–36.
- [32] Carpinteri A, Valente S. Numerical modeling of mixed-mode cohesive crack propagation. In: Atluri SN, Yagawa G, editors. *International conference on computational engineering science*. Springer Verlag; 1988. p. 12.vi.1–2.
- [33] Cen Z, Maier G. Bifurcations and instabilities in fracture of cohesive-softening structures: a boundary elements analysis. *Fatigue Fract Engng Mater Struct* 1992;15:911–28.
- [34] Elices M, Guinea GV, Planas J. Prediction of size-effect based on cohesive crack model. In: Carpinteri A, editor. *Size-scale effects in the failure mechanisms of materials and structures*. E & FN Spon; 1996. p. 309–24.
- [35] Carpinteri A. Fractal nature of material microstructure and size effects on apparent mechanical properties. *Mech Mater* 1994;18:89–101.
- [36] Carpinteri A. Scaling laws and renormalization groups for strength and toughness of disordered materials. *Int J Solids Struct* 1994;31:291–302.
- [37] Carpinteri A, Chiaia B, Ferro G. Size effects on nominal tensile strength of concrete structures: multifractality of material ligaments and dimensional transition from order to disorder. *Mater Struct* 1995;28:311–7.
- [38] Carpinteri A, Chiaia B. Multifractal nature of concrete fracture surfaces and size effects on nominal fracture energy. *Mater Struct* 1995;28:435–43.
- [39] Carpinteri JA, Chiaia B, Cornetti P. A scale-invariant cohesive crack model for quasi-brittle materials. *Engng Fract Mech* 2002;69:207–17.
- [40] Carpinteri A, Ferro G. Size effects on tensile fracture properties: a unified explanation based on disorder and fractality of concrete microstructure. *Mater Struct* 1994;28:563–71.
- [41] van Mier JGM, van Vliet MRA. Effect of strain gradients on the size effect of concrete in uniaxial tension. *Int J Fract* 1999;94:195–219.
- [42] Carpinteri A, Ingraffea AR, editors. *Fracture mechanics of concrete: material characterization and testing*. The Hague, Boston, Lancaster: Martinus Nijhoff; 1984.

- [43] Carpinteri A. Mechanical damage and crack growth in concrete: plastic collapse to brittle fracture. Dordrecht: Martinus Nijhoff Publishers; 1986.
- [44] Shah SP, Carpinteri A, editors. Fracture mechanics test methods for concrete. London, New York: Chapman & Hall; 1991.
- [45] Carpinteri A, editor. Applications of fracture mechanics to reinforced concrete. London, New York: Elsevier Applied Science; 1992.
- [46] Carpinteri A, editor. Size-scale effects in the failure mechanisms of materials and structures. London, New York: Chapman & Hall; 1996.
- [47] Carpinteri A, Aliabadi MH, editors. Computational fracture mechanics in concrete technology. Southampton, Boston: WIT Press; 1999.
- [48] Carpinteri A, editor. Minimum reinforcement in concrete members. Oxford: Elsevier Science; 1999.
- [49] Carpinteri A, editor. Nonlinear crack models for nonmetallic materials. Dordrecht, Boston, Lancaster: Kluwer Academic Publishers; 1999.
- [50] Carpinteri A. Development of realistic concrete models including scaling effects. Nuclear Science and Technology, Shared Cost Action (SCA) programme 1985–1987, Research Contract No. 3302-87-12 ELISPI, 1989.
- [51] Carpinteri A. Size effects on strength, toughness and ductility. *J Engng Mech (ASCE)* 1989;115:1375–92.
- [52] Elfgren L. Round-Robin analysis of anchor bolts. RILEM TC-90 FMA. Fracture Mechanics of Concrete—Applications. RILEM TC-90 FMA, 1991.
- [53] Carpinteri A. Notch sensitivity in fracture testing of aggregative materials. *Engng Fract Mech* 1982;16:467–81.
- [54] Carpinteri A. Application of fracture mechanics to concrete structures. *J Engng Mech (ASCE)* 1982;108:833–48.
- [55] Biolzi L, Cangiano S, Tognon G, Carpinteri A. Snap-back softening instability in high-strength concrete beam. *Mater Struct* 1989;22:429–36.
- [56] Standard method of test for plane strain fracture toughness of metallic materials. Technical Report E399- 74, ASTM.
- [57] Tada H, Paris P, Irwin G. The stress analysis of cracks handbook. St. Louis, MO: Del Research Corporation; 1963.
- [58] Colombo G, Limido E. A numerical method for the analysis of stable TPBT test: comparison with some experimental data. In: XI Convegno Nazionale per l'Analisi delle Sollecitazioni, Thrin; 1983. p. 233–43.
- [59] Determination of the fracture energy of mortar and concrete by means of three-point bending tests on notched beams. Technical Report 18, Materials and Structures (RILEM), 1985.
- [60] Bocca P, Carpinteri A, Valente S. Fracture mechanics of brick masonry: size effect and snap-back analysis. *Mater Struct* 1989;22:364–73.
- [61] Maier G, Cen Z, Novati G, Tagliaferri R. Fracture, path bifurcations and instabilities in elastic cohesive-softening models: a boundary elements approach. In: van Mier JGM, Rots JG, Bakker A, editors. Fracture processes in concrete, rock, ceramics. E & FN Spon; 1991. p. 695–704.
- [62] Carpinteri A, Sih GC. Damage accumulation and crack growth in bilinear materials with softening. *Theor Appl Fract Mech* 1984;1:145–59.
- [63] Cedolin L, Dei Poli S, Iori I. Tensile behaviour of concrete. *J Engng Mech (ASCE)* 1987;113:431–49.
- [64] Bocca P. Indagine teorico-sperimentale sulla determinazione della resistenza del calcestruzzo mediante prova di estrazione. *L'Industria Italiana Cemento* 1979;45–52.
- [65] Bocca P. The application of pull-out test to high strength concrete estimation. *Mater Struct* 1984;17:211–6.
- [66] Bocca P, Carpinteri A, Valente S. Evaluation of concrete fracture energy through a pull-out testing procedure. In: Swartz SE, Shah SP, Barr B, editors. Fracture of concrete and rock—recent developments. Elsevier Applied Science; 1989. p. 347–56.
- [67] Bocca P, Carpinteri A, Valente S. Fracture mechanics evaluation of anchorage bearing capacity in concrete. In: Carpinteri A, editor. Applications of fracture mechanics to reinforced concrete. Elsevier Applied Science; 1992. p. 231–65.
- [68] Valente S, Carpinteri A. Analysis of anchor bolts by the cohesive crack model. In: Elfgren L, editor. Round-Robin analysis of anchor bolts. RILEM TC-90 FMA Fracture Mechanics of Concrete—Applications. RILEM TC-90 FMA. 1991. p. 19.1–8.
- [69] Ferrara G, Morabito P. A contribution of the holographic interferometry to studies on concrete fracture. In: Shah SP, Swartz SE, Barr B, editors. Fracture of concrete and rock—recent developments. Elsevier Applied Science; 1989. p. 337–46.
- [70] Schlangen E, van Mier JGM. Boundary effect in mixed-mode I and II fracture of concrete. In: van Mier JGM, Rots JG, Bakker A, editors. Fracture processes in concrete, rock, ceramics. E & FN Spon; 1991. p. 705–16.
- [71] Carpinteri A, Ferrara G, Melchiorri G. Single edge notched specimen subjected to four-point shear: an experimental investigation. In: Shah SP, Swartz SE, Barr B, editors. Fracture of concrete and rock—recent developments. Elsevier Applied Science; 1989. p. 605–14.
- [72] Carpinteri A, Ferrara G, Melchiorri G, Valente S. The four-point shear test on single-edge notched specimen: an experimental and numerical analysis. In: Firrao D, editor. Eighth European Conference on Fracture, Torino. EMAS; 1990. p. 667–75.
- [73] Valente S. Heuristic softening strip model in the prediction of crack trajectories. *Theor Appl Fract Mech* 1993;19:119–25.
- [74] Schlangen E. Experimental and numerical analysis of fracture processes in concrete. PhD thesis, Delft University, The Netherlands, 1992.

- [75] Carpinteri A, Valente S, Ferrara G, Melchiorri G. Friction-toughness interaction for mixed-mode crack propagation in concrete. In: Rossmann HP, Miller KJ, editors. International Conference on mixed-mode Fracture and Fatigue. ESIS Publication, vol. 14. 1993. p. 171–83.
- [76] Barpi F, Valente S. Size-effects induced bifurcation phenomena during multiple cohesive crack propagation. *Int J Solids Struct* 1998;35(16):1851–61.
- [77] Arrea M, Ingraffea AR. Mixed-mode crack propagation in mortar and concrete. Technical Report 81-13, Department of Structural Engineering, Cornell University, 1982.
- [78] de Borst R. Non-linear analysis of frictional materials. PhD thesis, Delft University, The Netherlands, 1986.
- [79] Rots JG. Removal of finite elements in strain softening analysis of tensile fracture. In: Bažant ZP, editor. Fracture mechanics of concrete structure. Elsevier Publisher; 1992. p. 330–8.
- [80] Alfaiate J, Pires JB, Martins JAC. A finite element model for the study of crack propagation in concrete. In: Aliabadi MH, Cartwright DJ, Nisitani H, editors. Localized Damage II. Fatigue and Fracture Mechanics, vol. 1. Southampton, Boston: Computational Mechanics Publications; 1992. p. 261–80.
- [81] Carpinteri A, Valente S, Ferrara G, Imperato L. Experimental and numerical fracture modelling of a gravity dam. In: Bažant ZP, editor. Fracture mechanics of concrete structures. The Netherlands: Elsevier Applied Science; 1992. p. 351–60.
- [82] Valente S, Barpi F. On singular points in mixed-mode cohesive crack propagation. In: Aliabadi MM, Carpinteri A, Kaliszky S, Cartwright DJ, editors. Localized Damage III. Southampton: Computational Mechanics Publications; 1994. p. 167–74.
- [83] Barpi F. Numerical models for the study of cracking phenomena in dams. PhD thesis, Politecnico di Torino, 1996.
- [84] Bolzon G, Cocchetti G, Maier G, Novati G, Giuseppetti G. Boundary element and finite element fracture analysis of dams by the cohesive crack model: a comparative study. In: Bourdarot E, Mazars J, Saouma V, editors. Dam fracture and damage. The Netherlands: Balkema; 1994. p. 69–78.
- [85] Tinawi R, Ghrif F. An anisotropic damage model for the response of concrete gravity dams. In: Bourdarot E, Mazars J, Saouma V, editors. Dam fracture and damage. The Netherlands: Balkema; 1994. p. 21–30.
- [86] Pellegrini R, Imperato L, Torda M, Ferrara G, Mazza G, Morabito P. Physical and mathematical models for the study of crack activation in concrete dams. In: Bourdarot E, Mazars J, Saouma V, editors. Dam fracture and damage. The Netherlands: Balkema; 1994. p. 169–76.
- [87] Plizzari GA, Saouma VE, Waggoner A. Experimental study of concrete gravity dams in a centrifuge. In: Bourdarot E, Mazars J, Saouma V, editors. Dam fracture and damage. The Netherlands: Balkema; 1994. p. 93–102.
- [88] Renzi R, Ferrara G, Mazza G. Cracking in a concrete gravity dam: a centrifugal investigation. In: Bourdarot E, Mazars J, Saouma V, editors. Dam fracture and damage. The Netherlands: Balkema; 1994. p. 103–9.
- [89] Valente S, Barpi F, Ferrara G, Giuseppetti G. Numerical simulation of centrifuge tests on prenotched gravity dam models. In: Bourdarot E, Mazars J, Saouma V, editors. Dam fracture and damage. Rotterdam (The Netherlands): Balkema; 1994. p. 111–9.
- [90] Barpi F, Valente S. Numerical simulation of prenotched gravity dam models. *J Engng Mech (ASCE)* 2000;126(6):611–9.
- [91] Aassved Hansen E. Influence of sustained load on the fracture zone of concrete. In: van Mier JGM, Rots JG, Bakker A, editors. Fracture processes in concrete rock and ceramics. E & FN Spon; 1991. p. 829–38.
- [92] Zhou FP, Hillerborg A. Time-dependent fracture of concrete: testing and modelling. In: Bažant ZP, editor. Fracture mechanics of concrete structures. The Netherlands: Elsevier Applied Science; 1992. p. 906–11.
- [93] Zhou FP. Time-dependent crack growth and fracture in concrete, PhD thesis, Report TVBM-1011, Lund University of Technology, Sweden, 1992.
- [94] Carpinteri A, Valente S, Zhou FP, Ferrara G, Melchiorri G. Crack propagation in concrete specimens subjected to sustained loads. In: Wittmann FH, editor. Fracture mechanics of concrete structures. Germany: Aedificatio; 1995. p. 1315–28.
- [95] Carpinteri A, Valente S, Zhou FP, Ferrara G, Melchiorri G. Tensile and flexural creep rupture tests on partially-damaged concrete specimens. *Mater Struct* 1997;30:269–76.
- [96] Barpi F, Chillè F, Imperato L, Valente S. Creep induced cohesive crack propagation in mixed mode. In: Durban D, Pearson JRA, editors. Non-linear singularities in deformation and flow. The Netherlands: Kluwer Academic Publishers; 1999. p. 155–68.
- [97] Barpi F, Ferrara G, Imperato L, Valente S. Lifetime of concrete dam models under constant loads. *Mater Struct* 1999;32:103–11.
- [98] Barpi F, Valente S. Time-dependent fracture of concrete using fractional order rate laws. In: de Borst R, Mazars J, Pijaudier-Cabot G, van Mier JGM, editors. Fracture mechanics of concrete structures. Balkema Publishers; 2001. p. 153–9.
- [99] Barpi F, Valente S. Creep rupture in concrete structures: a new space and time integration scheme. In: Ulm FJ, Bažant ZP, Wittmann F, editors. Creep, shrinkage and durability mechanics of concrete and other quasi-brittle materials. Elsevier; 2001. p. 251–7.
- [100] Barpi F, Valente S. Creep and fracture in concrete: A fractional order rate approach. *Engng Fract Mech* 2003;70:611–23.
- [101] Barpi F, Valente S. Time-dependent fracture of concrete dam models with fuzzy parameters. In: Dubois D, editor. Fourth International Conference on Computing Anticipatory Systems (CASYS 2000), Liège, Belgium, August 7–12, 2000. 2000. p. 325–37.
- [102] Barpi F, Valente S. Fuzzy parameters analysis of time-dependent fracture of concrete dam models. *Int J Numer Anal Meth Geomech* 2002;26:1005–27.

- [103] Bažant ZP, Kim JK, Pfeiffer PA. Determination of fracture properties from size effect tests. *J Struct Engng (ASCE)* 1984;112:289–307.
- [104] Mandelbrot BB. *The fractal geometry of nature*. New York: W.H. Freeman & Company; 1982.
- [105] Feder J. *Fractals*. New York: Plenum Press; 1988.
- [106] van Mier JGM, van-Vliet MRA. Experimental investigation of size effect in concrete under uniaxial tension. In: Mihashi H, Rokugo K, editors. *Proceedings of FRAMCOS-9. Aedificatio*; 1998. p. 1923–36.
- [107] Carpinteri A, Chiaia B, Nemati KM. Complex fracture energy dissipation in concrete under different loading conditions. *Mech Mater* 1997;26:93–108.
- [108] Carpinteri A, Chiaia B, Invernizzi S. Three-dimensional fractal analysis of concrete fracture at the meso-level. *Theor Appl Fract Mech* 1999;31:163–72.
- [109] Carpinteri A, Cornetti P. Size effects on concrete tensile fracture properties: an interpretation of the fractal approach based on aggregate grading. *J Mech Behav Mater* 2002;13:233–46.
- [110] Carpinteri A, Chiaia B, Cornetti P. On the mechanics of quasi-brittle materials with a fractal microstructure. *Engng Fract Mech*, in press.
- [111] Carpinteri A, Chiaia B. Power scaling laws and dimensional transitions in solid mechanics. *Chaos, Solitons Fract* 1996;7:1343–64.
- [112] Carpinteri A, Chiaia B. Multifractal scaling laws in the breaking behavior of disordered materials. *Chaos, Solitons Fract* 1997;8:135–50.
- [113] Carpinteri A, Chiaia B, Ferro G. Scale dependence of tensile strength of concrete specimens: a multifractal approach. *Mag Concr Res* 1998;50:237–46.
- [114] Carpinteri A, Chiaia B. Size effects on concrete fracture energy: dimensional transition from order to disorder. *Mater Struct* 1996;29:259–66.
- [115] Carpinteri A, Chiaia B. Crack-resistance behavior as a consequence of self-similar fracture topologies. *Int J Fract* 1996;76:327–40.
- [116] Carpinteri A, Chiaia B, Ferro G. A new explanation for size effects on the flexural strength of concrete. *Mag Concr Res* 1997;49:45–53.
- [117] Carpinteri A, Ferro G, Monetto I. Scale effects in uniaxially compressed concrete specimens. *Mag Concr Res* 1999;51:217–25.
- [118] Konstantinidis A, Frantziskonis G, Carpinteri A, Aifantis EC. Size effects on tensile strength and fracture energy in concrete: wavelet vs. fractal approach. *J Mech Behav Mater* 2001;12:63–75.
- [119] Efraimidis G, Carpinteri A, Aifantis EC. Multifractal scaling law versus gradient elasticity in the evaluation of disordered materials compressive strength. *J Mech Behav Mater* 2001;12:107–20.
- [120] Carpinteri A, Cornetti P. A fractional calculus approach to the description of stress and strain localization in fractal media. *Chaos, Solitons Fract* 2002;13:85–94.
- [121] Carpinteri A, Mainardi F, editors. *Fractals and fractional calculus in continuum mechanics*. Wien: Springer-Verlag; 1997.
- [122] K.M. Kolwankar. *Studies of fractal structures and processes using methods of functional calculus*. PhD thesis, University of Pune, 1998.
- [123] Podlubny I. *Fractional differential equations*. San Diego: Academic Press; 1999.
- [124] Carpinteri A, Chiaia B, Cornetti P. A fractional calculus approach to the mechanics of fractal media. *Rend Seminario Matematico dell'Universiti e Politecnico di Torino* 2000;58:57–68.
- [125] Carpinteri A, Chiaia B, Cornetti P. Static-kinematic duality and the principle of virtual work in the mechanics of fractal media. *Comput Meth Appl Mech Engng* 2001;191:3–19.
- [126] Carpinteri A, Cornetti P, Kolwankar KM. Calculation of the tensile and flexural strength of disordered materials using fractional calculus. submitted for publication.
- [127] Carpinteri A, Ferro G. Scaling behaviour and dual renormalization of experimental tensile softening responses. *Mater Struct* 1998;31:303–9.
- [128] Kleiser T, Bocek M. The fractal nature of slip in crystals. *Z Metall* 1986;77:582–7.
- [129] Vallejo EL. *Fractal analysis of the fabric changes in a consolidating clay*. *Engng Geol* 1996;43:281–90.
- [130] Ferro G. *Effetti di scala sulla resistenza a trazione dei materiali*. PhD thesis, Politecnico di Torino, 1994.
- [131] van Vliet MRA. *Size effect in tensile fracture of concrete and rock*. PhD thesis, Technical University of Delft, 2000.